INSTRUMENTATION FOR X-RAY ASTRONOMY

BRIAN D. RAMSEY
Space Science Laboratory, NASA/George C. Marshall Space Flight Center, AL 35812, U.S.A.
ROBERT A. AUSTIN
Hughes STX, NASA/George C. Marshall Space Flight Center, AL 35812, U.S.A.
and
RUDOLF DECHER
Space Science Laboratory, NASA/George C. Marshall Space Flight Center, AL 35812, U.S.A.

(Received November 24, 1993)

Abstract. Less than five decades ago, the first X-ray observations of the sky were made using simple devices such as film and geiger counters with crude collimators. These instruments were carried aloft by sounding rockets and made observations lasting only a few minutes at most. Today, orbiting observatories, utilizing high-resolution CCDs at the focus of arc sec optics, have lifetimes measured in years. To maintain the pace of discovery in X-ray astronomy, detectors must continue to evolve into devices of ever increasing sensitivity and sophistication. Further progress depends upon a host of technologies: grazing incidence optics, proportional counters, semiconductors, calorimeters, etc. In this article we present a brief qualitative overview of these technologies and of the principles behind them, as well as some examples of how they are employed in scientific missions for X-ray observations at energies up to 100 keV.

Table of Contents

1. Introduction
  1.1. X-Ray Astronomy
  1.2. Observational Requirements
    1.2.1. Imaging
    1.2.2. Spectrometry
    1.2.3. Polarimetry
    1.2.4. Timing
2. Techniques
  2.1. Imaging and Flux Concentration
    2.1.1. Mechanical Non-Focusing Collimators
    2.1.2. Grazing Incidence Optics
      2.1.2.1. Traditional Grazing Incidence Optics
      2.1.2.2. Replicated Optics
      2.1.2.3. Foil Optics
      2.1.2.4. Microchannel Plate Optics
      2.1.2.5. Multilayer Coatings
    2.1.3. Flux Concentrators
    2.1.4. Coded Aperture Masks
  2.2. Dispersive Spectrometers
    2.2.1. Bragg Crystal Spectrometers
    2.2.2. Transmission Spectrometers
  2.3. Polarimeters
    2.3.1. Bragg Crystal Polarimeters
    2.3.2. Compton Scattering Polarimeters
    2.3.3. Photoelectric Polarimeters

Space Science Reviews **69:** 139–204, 1994.

- 2.4. Backgrounds and Shielding
- 3. Detectors
  - 3.1. Basic Principles
  - 3.2. Gas-Filled Detectors
    - 3.2.1. Introduction
    - 3.2.2. Proportional Counters
    - 3.2.3. Multiwire Proportional Counters
    - 3.2.4. Gas Scintillation Proportional Counters
  - 3.3. Microchannel Plates
  - 3.4. Semiconductor Detectors
    - 3.4.1. Introduction
    - 3.4.2. Slab with Ohmic Contacts
    - 3.4.3. PN Junctions
    - 3.4.4. PIN Detectors
    - 3.4.5. CCDs
  - 3.5. Calorimeters
  - 3.6. Superconducting Tunnel Junction Detectors
- 4. Conclusions

1. Introduction

1.1. X-RAY ASTRONOMY

The growth of our knowledge of the X-ray universe, as in other areas of experimental and observational science, has been dependent upon advances in detector technology, but with the additional complication that the opacity of the Earth's atmosphere to X-rays necessitates observations from satellites, rockets or high-altitude balloons. Since the first X-ray observations, made in the late 1940's, set out only to determine if X-ray sources existed in the sky, simple detectors sufficed – usually film or Geiger counters caried above the atmosphere by sounding rockets. After the discovery of the first extra solar X-ray source, Sco X-1 in 1962, it became apparent that many powerful extra-solar sources of X-rays existed, that some were extended (the Crab Nebula, for example), and that nearly all showed time variability on a variety of scales. To better measure these characteristics, effort went into designing detectors that had short response times and, in combination with collimators, arc min angular resolution. Some of the detectors that were built had moderate energy resolution (proportional counters) to good energy resolution (semiconductors). The detection of lines and absorption features in the X-ray spectra provided valuable information about the chemical composition and dynamics of celestial sources. The next step was to fly sensitive spectrometers (Bragg crystals and transmission gratings). During the 1970's, in parallel with these developments, came high resolution X-ray mirrors which, in combination with microchannel plate detectors, made arc sec imaging possible. The increase in signal-to-noise ratio provided by focusing grazing incidence optics resulted in a very large improvement in sensitivity. Presently, with CCD cameras, calorimeters, sub-arc sec X-ray optics, and other developments in X-ray telescope technology, we are poised to carry our investigations of the X-ray universe to a new level of detail.

Many celestial objects emit X-rays: stars, including of course the Sun, hot gas clouds, supernova explosions and remnants (such as neutron stars and black holes), galaxies, and quasars. In these sources, X-rays are generally thought to be generated by one or more processes, including the following: emission due to heating of gas accreted onto the surface of a compact object from a companion star (thermal bremsstrahlung); acceleration of charged particles in local magnetic fields (synchrotron radiation); electron-photon collisions (inverse Compton effect); and energy transitions in excited atomic nucleii. The former three processes generate continuum radiation whereas the latter is responsible for discrete lines.

1.2. OBSERVATIONAL REQUIREMENTS

In order to detect X-rays in the energy range of interest here (<100 keV), the detector absorbing material is usually chosen to ensure that photoelectric absorption is the dominant effect. This is done so that all the incident energy is initially deposited at a point in the detector; this makes possible the precise determination of incident energy and event location. The information carriers (electrons, holes, photons, or phonons) liberated by the photoelectric interaction are then collected to determine at least one of the following parameters: interaction location (imaging), energy (spectrometry), polarization of the incident X-rays, and arrival time.

1.2.1. Imaging

The capacity to image X-ray sources reduces the possibility of source confusion and often permits identification of sources with their visible, infrared, or radio counterparts. Imaging resolution of ideally an arc min or better is desirable for mapping out regions in clusters of galaxies, hot gas distributions, jets, and halos. For example, in the case of an extended source such as the Coma cluster, information about the quantity and distribution of hot intracluster gas can be used to determine magnetic fields, measure electron densities, and find evidence for large-scale mass motions. Such knowledge can ultimately be used to constrain cosmological models.

1.2.2. Spectrometry

X-ray spectroscopy, due to the relative simplicity of elemental spectra in the X-ray band, is an exceptionally powerful tool for performing diagnostic studies of X-ray sources and it can be used to determine physical parameters of emitting regions of all classes of X-ray emitters: stars, X-ray binaries, supernova remnants, galaxies, clusters of galaxies, and quasars, as well as interstellar and intergalactic material. Studies of emission lines provide temperatures, ionization states, densities, velocities, and elemental abundances. Absorption features provide similar information in cases where bright X-ray sources are enveloped in cooler, extended gas clouds which are ionized by the X-rays. With sufficiently high spectral resolution (~ 1000), measurements of line Doppler shifts would allow detailed studies of mass motions in supernova remnants, X-ray binaries, turbulent intra-cluster or intra-galactic gas, or early-type galaxies in clusters. The results of these measurements are synthesized into a picture of the structure and evolution of the X-ray source(s) under study.

1.2.3. Polarimetry

In an astrophysical context, polarization is expected to arise as a result of non-thermal emission mechanisms. These include synchrotron radiation; X-ray scattering such as from accretion disks; and the emission and propagation of X-rays in the extremely strong magnetic fields characteristic of neutron star sources such as pulsars. Cosmic X-ray sources such as supernova remnants, binary X-ray sources powered by accretion disks, black hole candidates and active galactic nuclei may all emit polarized X-rays. Subsets of these, such as the accretion disks, may have very large degrees of polarization according to current theoretical models.

The measurement of polarization adds additional information that can be folded into theoretical models. For example, quasars emit most of their energy in X-rays, but the origin of this radiation is unclear. It can be modeled equally well as emission from a disk, a torus, or a jet; but each of these models predicts quite different amounts of polarization, the measurement of which could help reveal the emission mechanisms. In the case of galactic sources such as pulsars, measurement of the X-ray polarization angle compared with that observed in the optical region can determine whether or not the pulsed emissions arise from the same synchrotron process or from totally different mechanisms (Meszaros *et al.*, 1988).

1.2.4. Timing

The X-ray sky is highly variable on all time scales – from milliseconds, characteristic of the innermost stable orbits of matter around black holes, to months in the case of X-ray transients. The desire for high time resolution data stems from the large amount of information that can be gleaned from them. Timing studies on extra-galactic objects, such as Active Galactic Nuclei (AGN) can be used to provide limits on the size of the emitting regions (from the light transit time) and hence provide limits on the masses of the central 'engines'. For galactic sources, period searches using Fast Fourier Transforms (FFT) can reveal the existence of pulsars, while measurements of their rate of change of frequency with intensity permits an investigation of the internal structure of the underlying neutron star. At the highest frequencies, analysis of millisecond variability provides a diagnosis of the inner regions of black holes, including measures of (quasi) periodicities from relativistic matter in the innermost stable orbits.

Any observation, be it imaging, spectrometry, polarimetry, timing or a combination of these measurements, will contain information about the source geometry and about the underlying physical processes occurring in the source being observed. These data can then be used to constrain existing physical models or provide fresh input for new models. As this process is iterative, ever more sensitive instruments and more sophisticated techniques are required to reveal new X-ray sources as well as to provide increasingly detailed observations of previously known ones. These techniques, and the associated detectors, are the subject of this review article. Section 2 covers the methods employed for accomplishing the types of observations outlined above, and Section 3 details the detectors necessary for their implementation.

2. Techniques

2.1. IMAGING AND FLUX CONCENTRATION

Techniques for imaging can be broken down into two broad categories. The first involves the use of mechanical collimators that either simply restrict the field of view to a narrow portion of the sky or modulate the source flux from the object of interest in a manner that is sky-position dependent. The second technique involves focusing optics, akin to optical astronomy, where X-ray mirrors bring the source flux to a focus on a position sensitive detector in the focal plane. The latter technique has found widespread use at low energies where X-rays can be easily reflected. The former technique, involving mechanical collimators, goes back to the earliest observations in X-ray astronomy, and is still in use today for higher energy observations.

2.1.1. Mechanical Non-Focusing Collimators

A simple mechanical slat or honeycomb collimator can be used at the entrance window of a detector to restrict the field of view as indicated in Figure 2.1. The field of view (α) depends on the length (L) and the width (a) of the apertures of the collimator ($\tan \alpha = a/L$). All photons arriving at angles larger than α are attenuated by the walls of the collimator structure. The angular response of the collimator has a triangular shape, and the angular width at the point where the source flux has dropped to 50% of its on-axis value, termed Full Width Half Maximum (FWHM), is a measure used to characterize the collimator response. With practical designs the field of view can be restricted to less than 1 deg, although for small openings the finite wall thickness becomes a significant fraction of each aperture width and reduces the instrument's effective area through obscuration.

If a mechanically collimated detector is mounted on a rotating platform (a spinning rocket or satellite) the angular position of a source in the scan direction can be determined from the detector response and platform pointing information with an accuracy dependent upon the detector's field of view. Repeating this process in several scan directions reveals the true location of the source on the sky. For improved angular resolution the field of view can be narrowed but at the cost of reduced observing time of a source per scan which leads to reduced sensitivity.

The first satellite devoted to X-ray astronomy, UHURU, had mechanical collimators constructed from aluminum tubes, of wall thickness 0.25 mm, glued together. Two types were flown: one constructed from 1.25 × 1.25 cm tubes, giving a field of view of $5 \times 5^\circ$ and the other from tubes 0.125 × 1.25 cm, having a field of view of $0.5 \times 5^\circ$. The spacecraft rotated at 0.08 RPM with the fine collimator

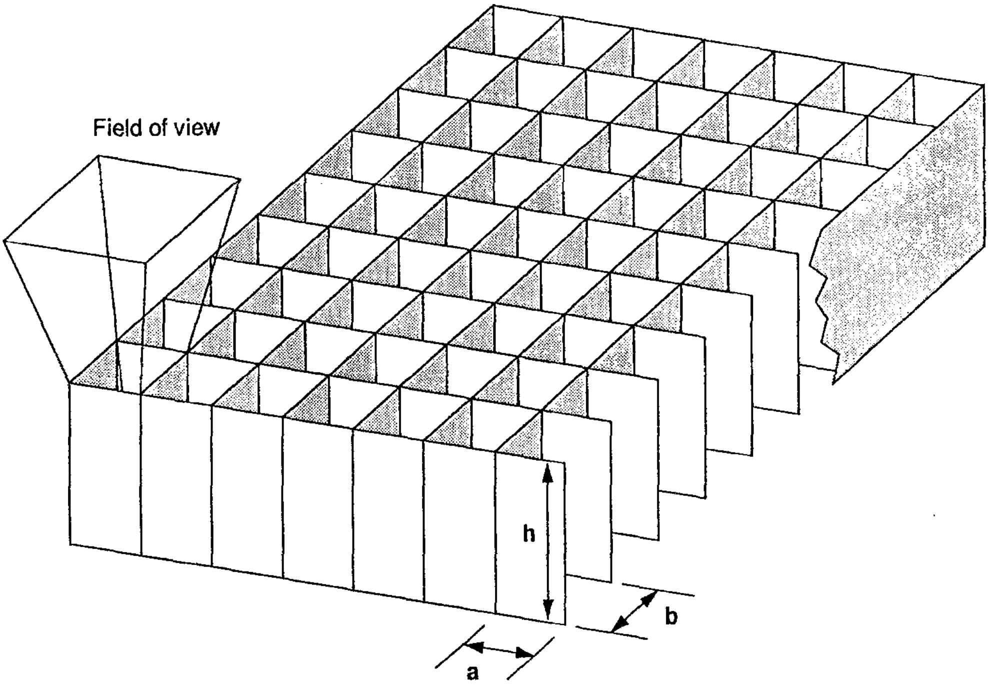

Fig. 2.1. A simple slat collimator of field of view $atan\ (a/h) \times atan(b/h)$ FWHM.

aligned in the direction of spin (Giacconi *et al.*, 1971). The angular resolution of UHURU was dependent upon the intensity of the source being observed and the extent to which it was confused by other nearby bright objects. For isolated strong sources, error boxes of width less than 1 arc min were possible in the scan direction.

Improved position determination can be achieved with a modulation collimator. First proposed by Oda (1965), the collimator consists of a pair of fine parallel grids which are situated above a detector and which define narrow planes of X-ray transmission on the sky (see Figure 2.2(a)). Scanning across a source, the flux is modulated by the transmission bands of the collimator, and the source position can be recovered with high accuracy from a precise knowledge of the collimator response function. Because there are multiple transmission bands, the field of view is not limited by the angular resolution of the collimator, as was the case for the simple slat collimator, and so scanning sensitivity is significantly enhanced. A modulation collimator operating over an approximately 1–10 keV range was flown aboard HEAO-1 (A3 experiment) in 1977 and gave angular resolutions of down to $\approx$10 arc sec for bright X-ray sources (Gursky *et al.*, 1978).

A variation of the modulation collimator technique is the Rotation Modulation Collimator (RMC). If the collimator is rotated about the pointing axis, as shown in Figure 2.2, the signal strength from a source in the field of view will be modulated as the source is alternately exposed to the detector or eclipsed by the grids. A point

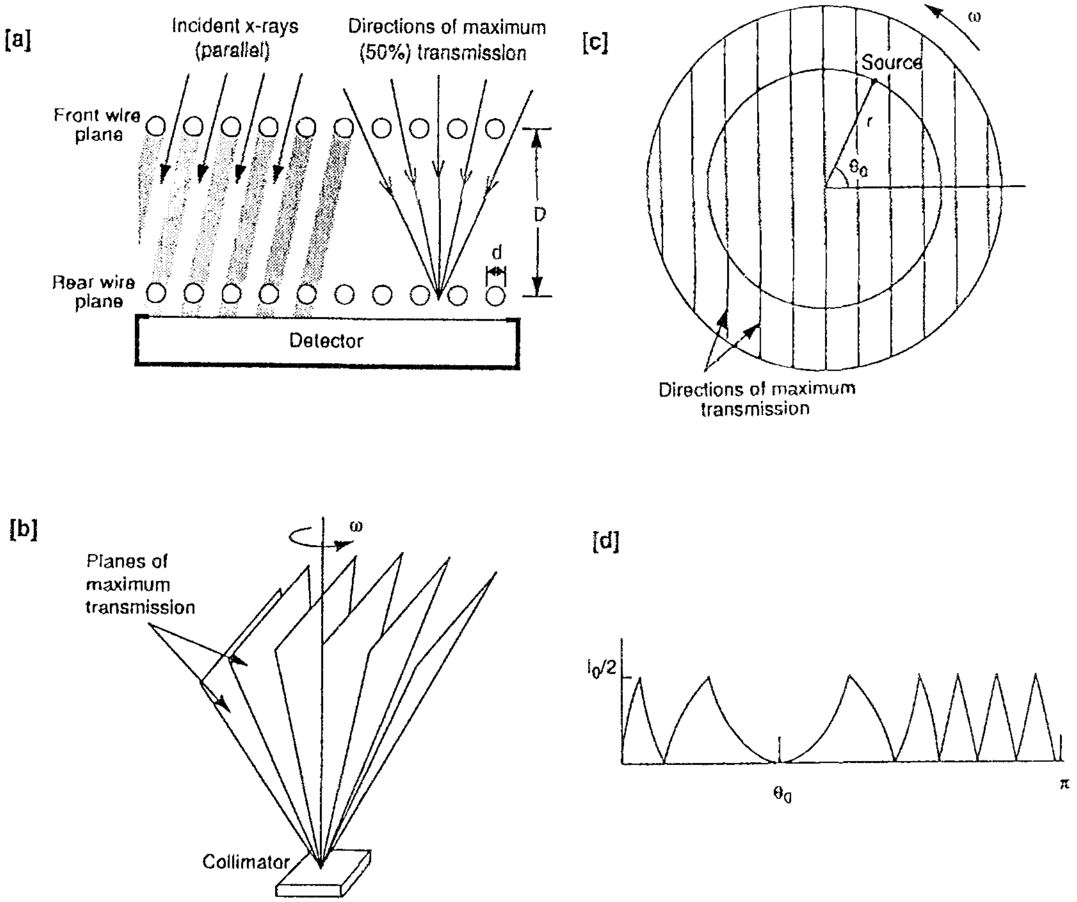

Fig. 2.2. The principle of the rotation modulation collimator. Wire grids define planes of transmission on the sky (a) which, when rotated (b), cause the source flux to be modulated in a location-dependent manner (d).

source located on the spin axis will not be modulated while the flux from an off-axis source will be modulated with a frequency dependent upon the angular distance from the axis. The time phase of the modulation provides the remaining angular coordinate (Schnopper *et al.*, 1968).

The attraction of the RMC technique over a scanning instrument is that the RMC observes the source field continuously and so greatly increases sensitivity. Also, many sources can be present in the field of view and subsequently deconvolved from the data. Typically, the data are analyzed using a cross-correlation technique which compares the observed modulation pattern with that expected from sources at trial positions in the field of view. Trial patterns are generated for given radial angles and are phase shifted to explore all azimuthal positions (Cruise and Willmore, 1979). The first RMC in orbit was flown aboard the British Ariel 5 satellite in 1974, and later devices were used on the SAS-3 satellite, launched in 1975. SAS-3 had a pair of RMCs, of differing angular resolution, and operated over the energy range 2–11 keV. For bright sources near the center of the 12° field of view, position accuracies of down to 20 arc sec were possible (Doxsey *et al.*, 1977).

Rotation Modulation Collimators are still being used, particularly for high-energy work where grazing incidence optics (2.1.2) cannot be employed. Despite being unusable for extended sources, whose fluxes are not modulated by the grids, it remains an attractive technique due in part to the fact that it does not require an imaging detector. Currently, there are at least 2 balloon-borne payloads utilizing the RMC technique for X-ray/gamma ray imaging. One is the FOBET instrument (Cardini *et al.*, 1992), which utilizes an array of 16 collimators, each above a solid scintillator detector (for a review of gamma ray detectors see Bertsch *et al.*, 1988), to give 22 arc min angular resolution in the energy range 20–300 keV. Another is the HEIDI experiment, intended for solar observations over the energy range 20 –700 keV, which has dual fine-pitch RMCs, also above solid scintillator detectors, giving 11 arc sec and 22 arc sec angular resolutions (Crannell *et al.*, 1991).

2.1.2. *Grazing Incidence Optics*

A very large increase in sensitivity can be obtained through the use of X-ray optics. By focusing the source photons to a small area on the detector plane the background is reduced by many orders of magnitude, and a point is quickly reached where the observation becomes limited only by the statistics of the source photons themselves. In addition, the ability to focus X-rays permits the use of small high-performance detectors, such as CCDs or calorimeters (see Section 3), which are not available in large area configurations.

The realization of such X-ray mirrors is only possible if the X-rays can be reflected. Fortunately, X-rays can undergo nearly total external reflection from surfaces at very small 'grazing' angles. The critical grazing angle θ_c, below which reflection can occur, can be calculated from dispersion theory. Away from any absorption edges, it is approximately given by

$$\theta_c = (4\pi r_0 \lambda^2 n)^{0.5} , \tag{1}$$

where r_0 is the classical electron radius, n is the electron density and λ the X-ray wavelength (Aschenbach, 1985). The largest critical angles are therefore obtained at low X-ray energies (long λ) and with dense reflectors as shown in Figure 2.3, which gives grazing angles as a function of energy for different elements. When these conditions are met then the phenomenon of total external reflection can be used to construct X-ray mirrors as focusing and imaging devices. As the grazing incidence angles are typically only a degree or so the effective (projected) reflecting surface is quite small. Nevertheless, by careful design, including nesting of the reflecting surfaces, large effective areas can be obtained, bringing a vast increase in sensitivity and image quality over non-focusing instruments.

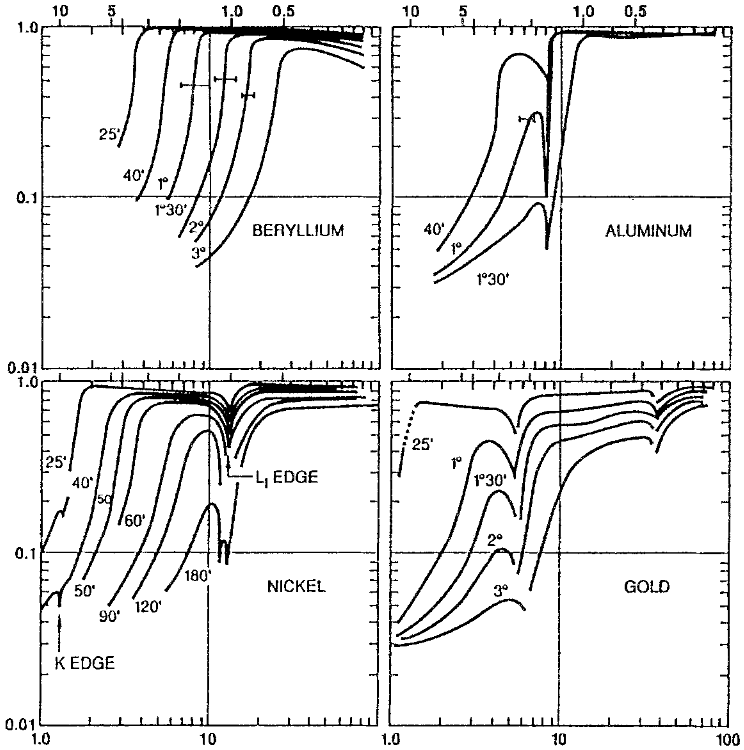

Fig. 2.3. X-ray reflectivities versus energy for several materials and grazing angles (from Zombeck, 1990). Energy (x axis) is shown in keV at the top, and the equivalent wavelength (Angstrom) at the bottom.

2.1.2.1. 'Traditional' Grazing Incidence Optics. Very high angular resolutions, at the arc sec level and below, have been achieved with grazing incidence X-ray optics used in conjunction with a position-sensitive detector in the focal plane. In a typical X-ray telescope (e.g., a Wolter Type I telescope – see Aschenbach (1985) for a review of X-ray telescope designs), reflections from two surfaces are used to form an X-ray image. The incoming photons are first reflected by a parabolic mirror, which concentrates off-axis rays into an annulus, and then by a hyperbolic mirror, which brings the annulus to a point in the focal plane. These mirrors are relatively thin cylindrical shells with the inner surface having the shape of the paraboloid or hyperboloid. To increase the effective collecting area, several pairs of parabolic and hyperbolic mirrors can be nested (Figure 2.4).

The fabrication of grazing incidence optics requires extremely precise figuring and high-quality surfaces. The mirrors are typically constructed from a low expansion material such as Zerodur, a glass ceramic, and are ground to a coarse figure contour. Fine lapping and polishing are then performed to give the final figure and the desired high-quality surface finish, typically better than 1 nm r.m.s. roughness for modern mirrors. The image quality depends critically on the figure of

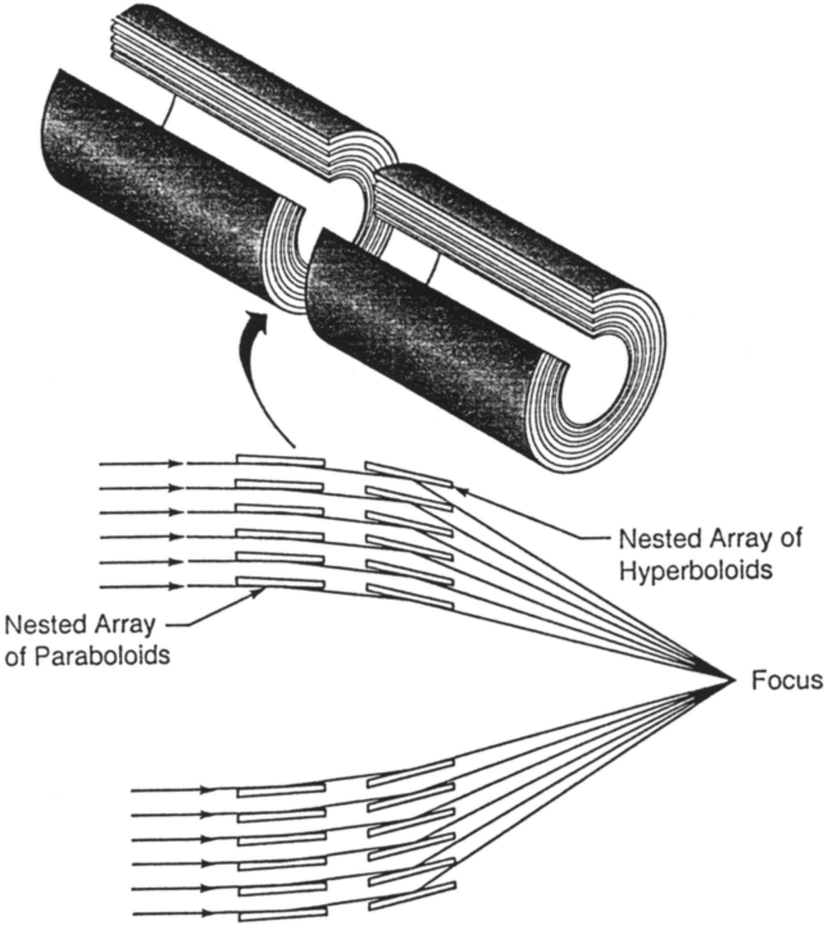

Fig. 2.4. A Wolter-1 mirror configuration showing nested paraboloids and hyperboloids.

the mirror, the alignment of the segments, and the final surface quality. The latter is of particular importance at short wavelengths where surface scattering dominates. Thus, while some early mirrors had high angular resolution as traditionally defined (Full Width at Half Maximum height of the response function, (FWHM)), only a small fraction of the reflected flux actually appeared within this radius; the rest appearing in broad wings of the point spread function (to better quantify the mirror quality the term Half Power Diameter (HPD) is now preferred. This is defined as the angular diameter in the focal plane in which half of the reflected rays fall. For 'poor-quality' mirrors the HPD can be much larger than the FWHM angular resolution).

X-ray telescopes produced using this traditional fabrication technique have been flown on several satellites and new telescopes for future space observatories are under development. The Einstein Observatory (HEAO-B), launched in 1978, carried an X-ray telescope with four nested mirror pairs which had an effective area of 400 cm^2 at 2.5 keV (40 cm^2 at 4 keV). The telescope had a focal length of 3.4 m, a field of view of 1° and a FWHM angular resolution of $\approx$4 arc sec. The mirrors were made from fused silica, finished to around 2.5 nm r.m.s. and coated with a nickel-chrome alloy.

Since this time much progress has been made in mirror technology and metrology, and recent mirrors have exhibited very low surface roughness. The German ROSAT satellite carries grazing incidence telescopes which have an effective area of around 1000 cm^2 at 0.2 keV, a surface roughness of better than 0.3 nm r.m.s. (Aschenbach, 1987), and an angular resolution of a few arc sec, while the optics being developed for the Advanced X-Ray Astrophysics Facility (AXAF-I) will have an angular resolution of better than 0.5 arc sec on axis (Van Speybroeck, 1987). AXAF-I, currently scheduled to fly in the late 1990s, will have the largest grazing incidence optics ever built, with an outer diameter of 1.2 m and a segment length of 0.84 m. The mirrors will be made from Zerodur, of maximum thickness 3.8 cm for the outer of the 4 nested shells, and will have a total weight of several thousand pounds. AXAF-I will have smaller grazing angles than ROSAT, to give increased response at higher energies, and will have a surface roughness of better than 0.7 nm r.m.s.. A Verification Engineering Test Article (VETA) was recently fabricated to develop the technology and, equally important, the metrology for production of the sub-arc second flight mirrors. VETA is the uncoated outermost hyperbolic/parabolic shell of the AXAF optic and was tested in the 500 m long facility at NASA/MSFC. After correcting for gravitational distortions, the optics was found to have a FWHM angular resolution of 0.22 arc sec at 1.5 keV and a HPD of better than 1 arc sec, meeting the goal for the flight assembly (see Weisskopf, 1992, and references therein). The advance in technology with the AXAF mirror is evident through a comparison of this HPD with the 16 arc sec HPD achieved with the (much smaller) Einstein mirror, which was itself considered a superb optic at the time. Specifications of the Einstein, ROSAT and AXAF mirrors are given in Table 2.1 and the testing of the VETA is shown in Figure 2.5.

The telescopes above represent the traditional approach wherein ultra-high-quality mirrors are meticulously fabricated to arc sec figure accuracy and ultra-smooth surface finish through machining, lapping and polishing. These mirrors return superb performance, but in an effort to avoid the high cost necessarily incurred with this type of labor-intensive work, and the large weight of these mirrors and their bulky support structure (which also severely limits the aperture filling factor), other schemes have been investigated to produce X-ray optics which trade angular resolution for increased throughput (particularly at higher energies), lighter weight, ease of construction and, as a direct consequence, considerably lower fabrication costs (Ulmer, 1989).

2.1.2.2. Replicated Optics. The replicated optics technique is a process for producing multiple thin mirror shells from a single shaped and polished mandrel. Each shell is built up on the surface of the mandrel, which has the negative figure of the

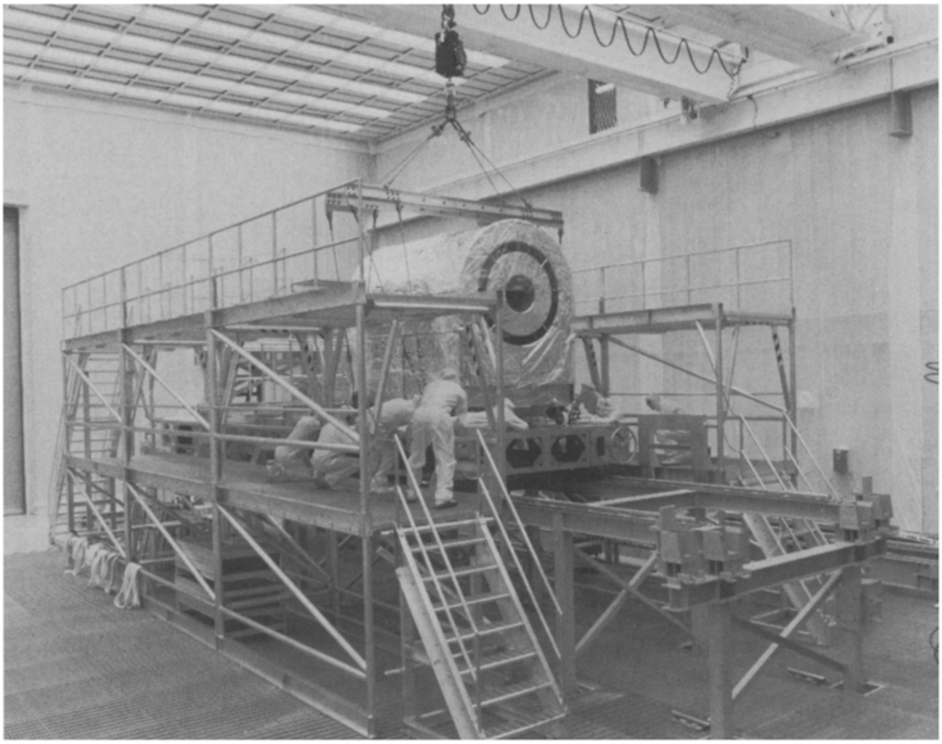

Fig. 2.5. Preparations for testing the AXAF Verification Engineering Test Article (VETA), shown center.

TABLE 2.1
Characteristics of the *Einstein*, ROSAT, and AXAF Wolter-1 mirrors (from Van Speybroeck, 1987)

	Einstein	ROSAT	AXAF
Number of mirror pairs	4	4	4
Outer diameter	0.6 m	0.8 m	1.2 m
Segment length	0.56 m	0.50 m	0.84 m
Geometric area	412 cm^2	1150 cm^2	1150 cm^2
Grazing angles	40–70 arc min	65-145 arc min	27–51 arc min
Focal length	3.4 m	2.4 m	10.0 m
Surface finish	2.5 nm r.m.s.	0.3 nm r.m.s.	0.7 nm r.m.s.
Half-power diameter	16 arc sec	5 arc sec	<1 arc sec

desired optic, and is then removed from the mandrel, usually by making use of the large difference in thermal expansion between the two components. No additional polishing or figuring of the shells takes place. The technique has considerable merit in that many shells can be fabricated for a single figuring and polishing of the mandrel, and the resulting shells can be very thin, which in turn permits high filling factors (de Korte, 1987).

There are several techniques currently in use for producing replicated X-ray optics. Each utilizes a correctly figured (negative) mandrel, usually made of glass or nickel-coated aluminum, which is either super-polished to a high surface finish (ideally less than 1 nm r.m.s.), or polished to around 5 nm and then overcoated with an acrylic lacquer to smooth out the residual roughness. The replication process then proceeds in one of several ways. In electroforming, the bare or lacquer-coated mandrel is first vacuum coated with a layer of gold, typically $\approx$100 nm thick, followed by an electrolytic nickel deposition of thickness typically $\approx$1 mm or less depending upon the diameter of the particular mirror segment. The whole assembly is then cooled, and the replica, consisting of the nickel shell coated with gold, separates from the master to which the gold was only poorly adhered. For added rigidity, particularly in large diameter mirror segments, the thin shell can be reinforced with light-weight epoxy.

Typical sources of error in the electroforming process are: departures of the initial mandrel from the desired figure; surface roughness of the mandrel; errors in the support structure from shell to shell; and stress build-up in the electroformed shell which distorts the figure. The latter implies a trade-off between thick and sturdy shells to preserve figure, and thin shells to give high packing density (high throughput).

Several proposed missions now include nickel electroformed replicated optics as their baseline mirrors. The European JET-X experiment, scheduled to fly on the Spectrum-X-Gamma satellite, has a pair of nested mirror assemblies in a Wolter-1 configuration giving a total effective area of 140 cm^2 at 8 keV (Wells *et al.*, 1991). By using relatively 'thick' nickel shells (around 1 mm) and super-polishing the mandrel to around 0.7 nm r.m.s., an angular resolution of 20 arc sec half-power diameter (HPD) is expected at 1.5 keV (Citterio *et al.*, 1991). For the Italian SAX mission, angular resolution has been traded for ease of fabrication of the mandrel by utilizing a conic approximation to the Wolter-1 geometry and much thinner mirror shells. Each mirror unit, of which there will be four, consists of thirty nested shells of thickness 0.2 mm (inner shell) to 0.4 mm (outer shell), giving a total weight of only 13 kg for each assembly including support structure. The resulting angular resolution will be around 2 arc min HPD (Citterio *et al.*, 1990). Details of the proposed JET-X and SAX optics are given in Table 2.2.

The European cornerstone high-throughput mission XMM is also scheduled to utilize replicated optics. Three identical telescopes are proposed, each having 58 nested Wolter-1 mirrors, giving a total effective area of 2000 cm^2 at 2 keV. The design goal is better than 30 arc sec angular resolution at 8 keV. Because of the

TABLE 2.2
Characteristics of the SAX (Citterio *et al.*, 1990) and JET-X (Citterio *et al.*, 1991) electroformed nickel replicated mirrors

	SAX	JET-X
Mirror type	Conical approximation to Wolter-1	Wolter-1
Number of telescopes	4	2
Shells per telescope	30	12
Outer shell diameter	15 cm	15 cm
Shell thickness	0.2–0.4 mm	0.7–1.1 mm
Focal length	1.85 m	3.5 m
Effective area	176 cm^2 at 7 keV	140 cm^2 at 8 keV
Half-power diameter	2 arc min	20 arc sec at 1.5 keV
Energy range	0.1–10 keV	0.3–10 keV

high packing density required, electroformed shells are being investigated with thicknesses ranging from 1.2 mm for the outer 35 cm diameter shell to 0.4 mm for the inner 16 cm diameter shell (Citterio *et al.*, 1992). The total length of each shell will be 60 cm and the focal length around 7.5 m. Individual electroformed mirror shells of different thickness and diameter have been fabricated and tested and exhibit the desired angular resolution for single units (18 arc sec at 8 keV) (Citterio *et al.*, 1992). However, because weight is a primary consideration, other techniques, such as epoxy replication, capable of producing even lighter structures, are also being studied in parallel.

An alternative approach, utilized on the European EXOSAT X-ray satellite mirrors (de Korte *et al.*, 1981)) and also investigated for the XMM optics (de Korte, 1987), is that of epoxy replication. Here, a high-quality mandrel is fabricated and coated with the desired reflecting surface, as in the electroforming process, but now a high-quality carrier is also fabricated separately with an identical, but positive, shape and of a slightly larger size than the mandrel. During the replication process, the carrier is brought up to the mandrel and 20–30 μm of epoxy is injected between the two. After curing under pressure the carrier is released from the mandrel through differential thermal expansion. For the EXOSAT mirrors (see Table 2.3), the mandrels were fabricated from Schott glass and the carriers were of beryllium, 3.5 mm thick. The reflective coating was evaporated gold. What makes the epoxy replication technique so attractive is the extremely light weight mirrors that can be produced. In the case of EXOSAT the complete mirror assembly weighed only 7 kg! For XMM, a carbon fiber reinforced epoxy is being investigated as the carrier material with thickness 0.6 mm for the inner shells to 1.4 mm for the outer mirror shells. The use of carbon fiber, *if successful*, could reduce the mirror assembly weight by up to a factor of three over the equivalent electroformed nickel optics (de Korte, 1987).

TABLE 2.3
Characteristics of the EXOSAT epoxy replicated mirrors (de Korte *et al.*, 1981)

Mirror type	Wolter-1
Number of mirror assemblies	2
Outer diameter	28 cm
Focal length	1 m
Number of shells per assembly	2
Shell material	Beryllium, 3.5 mm thick
Geometric area per assembly	91 cm^2
Half-power diameter	30 arc sec @ 1 keV
Weight	7 kg

2.1.2.3. Foil Optics. At shallow grazing angles the precise figure of the Wolter-1 optic can be approximated by two conic sections, with little loss of image quality. These sections can be fabricated from very thin bent foils which, because of their lack of bulky backing material, can be densely packed to give very high aperture filling factors. The Broad Band X-Ray Telescope (BBXRT) is such an optical system, flown on the space shuttle in 1990 for X-ray imaging in the 0.5–12 keV energy band (Serlemitsos *et al.*, 1984). It consisted of two identical conical mirror assemblies, each having 101 reflectors of 125 μm aluminum foil coated, by dipping, with 10 μm of acrylic lacquer to provide a smooth surface finish and then overcoated with 50 nm of gold, by vacuum deposition, to provide the X-ray reflectivity. The angular resolution (HPD) was around 4 arc min, set primarily by the accuracy of placement, and the surface quality, of the individual bent foils.

The fabrication of foil mirrors is greatly simplified by the fact that each and every reflector of the nested array can be made from different lengths of the same annulus (Petre and Serlemitsos, 1985). Thus the reflectors can be mass produced at very low cost and this is a key element of the foil mirror design. Each reflector is arranged so that its top edge is at the same radial distance from the optical axis as the lower edge of the next outer one, so that no part of a reflector is occulted by any other for on-axis flux. A precision machined alignment/support bar with tapered slots holds each reflector in place with just enough freedom of movement to permit easy insertion of the foils without the risk of damage. The tight packing of very thin substrates ensures high filling factors; about 70% for BBXRT, compared to around 14%, for example, in the case of the AXAF-I Wolter-1 mirrors. The use of ultra-thin foils also results in a very light-weight assembly, around 20 kg for each of the BBXRT mirrors.

BBXRT-type foil mirrors are currently flying on the Japanese ASCA mission and others are being developed for the SODART telescope on board the Russian Spectrum-X-Gamma spacecraft. Details of these are given in Table 2.4 below and an ASCA foil mirror assembly is shown in Figure 2.6.

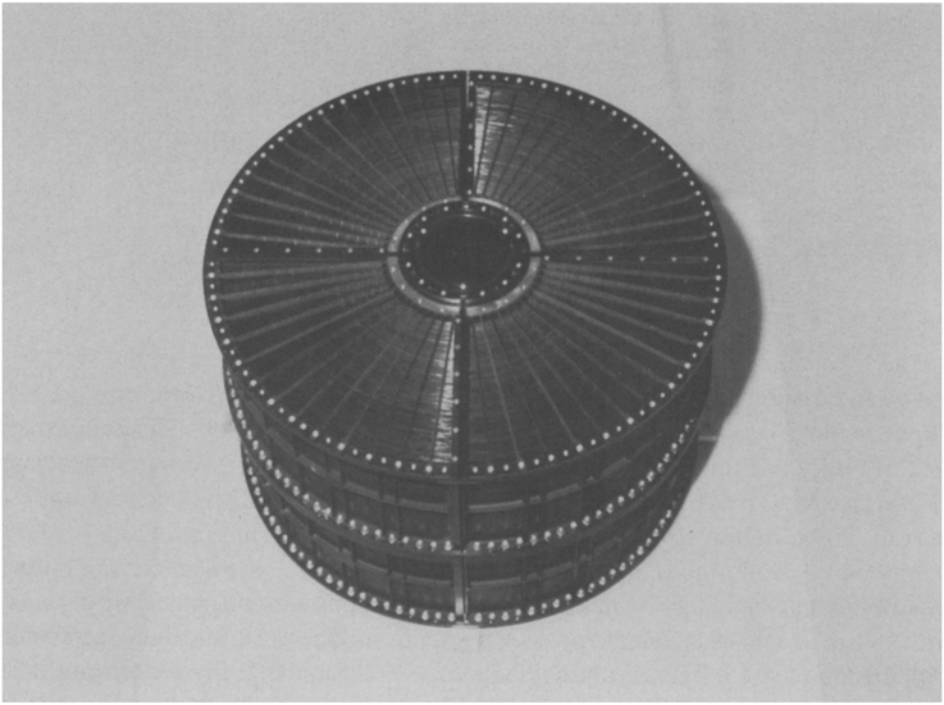

Fig. 2.6. One of the four foil mirror assemblies on board the ASCA spacecraft (courtesy of Pete Serlemitsos, Goddard Space Flight Center).

TABLE 2.4
Details of conical foil mirror assemblies for the ASCA and Spectrum-X-Gamma (Westergaard *et al.*, 1990) missions.

	ASCA	SODART
Number of mirror assemblies	4	2
Number of shells per mirror	120	154
Foil	0.125 mm, aluminum	0.3 mm, aluminum
Outer diameter	35 cm	60 cm
Total effective area	600 cm^2 at 7 keV	1200 cm^2 at 7 keV
Focal length	3.5 m	8 m
Energy range	0.5–20 keV	0.5–20 keV
Half-power diameter	3.5 arc min	4 arc min

Further developments of foil optics include the use of an epoxy replication process, in place of the lacquer dipping, to give a smoother surface finish to the foils. A series of high-surface-quality cylinders is fabricated, coated with gold, and dipped in epoxy. The aluminum foils are then wrapped around the cylinders, the epoxy cured, and the foils pealed off taking the high-quality gold finish with them. Early results from these foil mirrors look extremely promising with much lower scattering wings in the response function (Serlemitsos, private communication). These optics could approach the theoretical resolution limit for the conical approximation to the Wolter-1 geometry ($\leq$0.5 arc min).

2.1.2.4. Microchannel Plate Optics. Many of the optics described above have the drawback that mechanical considerations dictate a rather large separation ($\approx$ mm) between reflecting surfaces, which could otherwise be packed much more tightly. If useful collecting areas are required, then large structures must be fabricated, and this in turn dictates large focal lengths, particularly at high energies where grazing angles are very small. To overcome this limitation several groups have recently begun investigating the use of microchannel plates (MCP, see Section 3.2.2) as focusing optics, as these offer the benefit of closely packed reflecting surfaces (10 –100 mm^{-1}) necessary for high throughput optics (Wilkins *et al.*, 1989; Fraser *et al.*, 1991; Kaaret *et al.*, 1992).

Figure 2.7(a) illustrates the concept for a planar MCP. X-rays incident on the plate surface, in this case from a point source, undergo total external reflection from channel walls and, for an odd number of reflections, are brought to a point focus. Those which scatter an even number of times emerge parallel to the incident ray. In addition, there is also a straight-through (unreflected) component. Extending this to two dimensions, with optimal square section channels, produces an image with several components: a point-focused component from an odd number of reflections in each plane; a cruciform resulting from an odd/even combination of reflections; and a diffuse component from an even number in each plane (Fraser *et al.*, 1991). To focus a parallel beam of X-rays necessitates changing the figure of the MCP. Figure 2.7(b) shows a so-called ‘lobster eye’ arrangement where X-rays are brought to a focus on a surface of radius one-half of that of the radius of curvature of the MCP. Such a configuration has been suggested for use as an all sky monitor (Angel, 1979; Fraser *et al.*, 1991) and the successful figuring or ‘slumping’ of MCPs has already been demonstrated (Fraser *et al.*, 1993). To date, the limiting factors in the development of MCP optics appear to be the relative alignment of the channels, which has restricted the angular resolution to $\approx$10 arc min, and the micro roughness of the channel surfaces which has resulted in relatively low efficiencies (a few percent at 10 keV). Both areas are being actively investigated. One scheme to improve alignment and surface quality for lobster eye lenses involves micro machining the reflecting channels in silicon by utilizing a photolithographic process with a chemical etch which proceeds at widely different rates for the different crystal planes (Chen *et al.*, 1993). By etching in a preferred

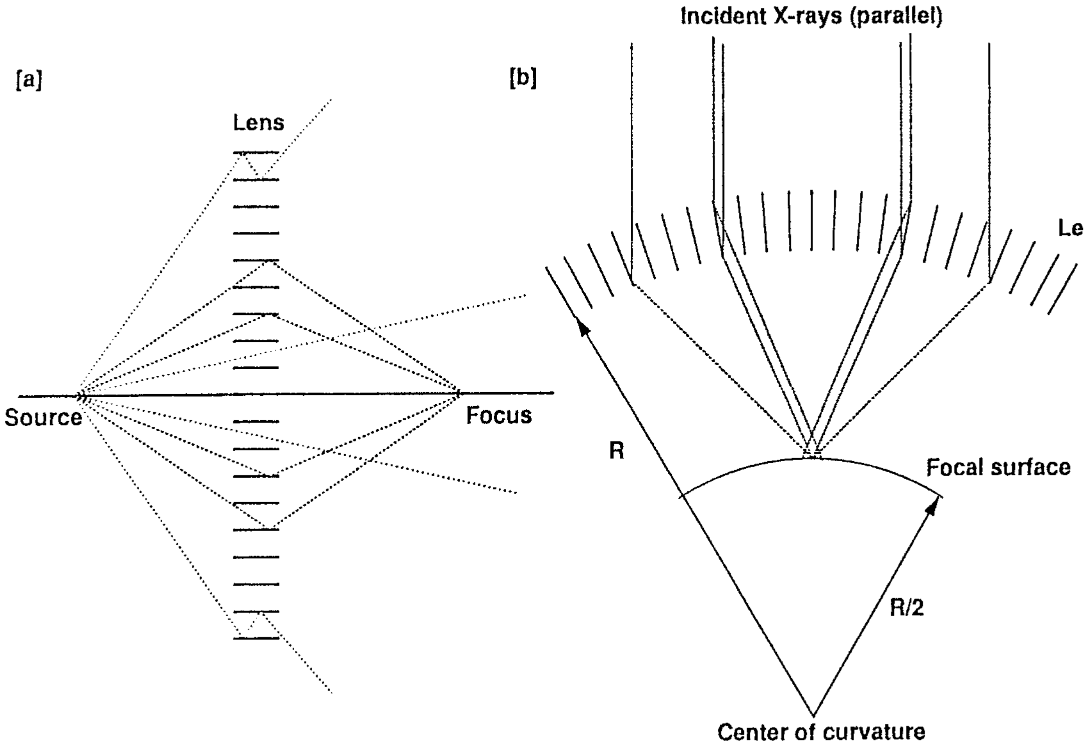

Fig. 2.7. The principles of microchannel plate optics. Only rays that scatter an odd number of times are brought to focus (a). Others are scattered from the beam or pass through without interaction. If the MCP is curved as in (b) then a lobster eye focusing device can be formed for wide field of view coverage.

direction, narrow channels are produced which are all automatically aligned with the structure of the crystal lattice, and this gives a very high degree of uniformity together with the possibility of improved surface quality, as micro machining can, in theory, give surface finishes down to a level of a few Angstroms.

2.1.2.5. Multilayer Coatings. In all of the above X-ray mirrors the high energy cut-off is set by the energy dependence of the critical angle which quickly leads to vanishingly small projected areas above 10–20 keV. To extend reflectivity to higher energies, the concept of graded multilayers has been proposed. In these, a series of bilayers, of alternating high Z/low Z materials with very different refractive indices, is deposited to give first order Bragg reflection (see Section 2.2.1) at angles above the critical angle. Constructive interference takes place between successive bi-layers with the same spacing, d, and, for a given angle of incidence, the coating can be tuned to give very high reflectivity at a *specific energy*. A normal incidence multilayer telescope, utilizing 45 identical bi-layers of molybdenum and silicon, has already been flown on a sounding rocket for observations of the solar emission from highly ionized iron in the range 17.1 to 17.5 nm (Walker *et al.*, 1988). An extension of this concept for broad-band coverage, by gradually varying the spacing between successive layers to give overlapping reflection components at different energies, has been variously proposed (Heavens and Liddell, 1966) and recently investigated for hard X-ray imaging (Christensen *et al.*, 1991). These so-called continuously graded multilayers have been fabricated on test flats with a large number of bilayers (up to 500–600) varying in thickness from d $\approx$1 nm to $d \approx$ 10 nm to give broad band reflectivity from 10 keV up to nearly 100 keV (Joensen *et al.*, 1993). The bilayers are arranged with the thinnest layers, providing high energy response, at the bottom and the thickest, providing low energy response, at the top. In this way the effects of X-ray absorption are minimized.

Key issues still to be addressed for this relatively new technology are build-up of stresses in the substrate materials and techniques for coating complex shapes with a high degree of uniformity. The former could prove the most serious challenge as typical coating processes, such as sputtering, tend to induce large stresses as the number of layers increases and these stresses deform the thin substrates necessary for high throughput optics. Techniques must be devised for reducing these stresses before useful hard X-ray optics can be fabricated.

2.1.3. Flux Concentrators

There is another class of X-ray optic which does not immediately provide imaging capability, but concentrates flux to give signal to noise advantage. One such device is the Kumakhov lens which relies on the phenomenon of total external reflection to transmit X-rays through minute circular glass capillaries. These capillaries can then be bent and, provided that certain critical angles are not exceeded, the beam will emerge traveling in a new direction. Although multiple reflections take place along the inside of the capillary, the tiny grazing angles ensure high reflectivity and thus high efficiency, despite large total angular deviations. By combining large numbers of capillaries into tapering bundles, ‘lenses’ can be fabricated that focus a parallel beam of X-rays to a common point. Such a device has been fabricated and demonstrated as an X-ray concentrator (Kumakhov, 1990); but the technology is still in its infancy, and there is, as yet, no known development program for hard X-ray astronomy.

2.1.4. Coded Aperture Masks

The coded aperture technique is a variant on the simple pinhole camera that overcomes the limitation of the single pinhole opening by replacing it with multiple apertures in a coded mask (Dicke, 1968). The mask consists of a pattern containing opaque and transparent areas (pixels). Radiation passing through the mask is spatially modulated by the mask pattern function and casts a shadow of the mask pattern on a position-sensitive detector located beneath the mask, as depicted in Figure 2.8. Radiation from different points in the field of view arrives at different angles (at the detector), each producing a shifted shadow pattern on the detector. The image of the source can then be reconstructed by deconvolving the recorded

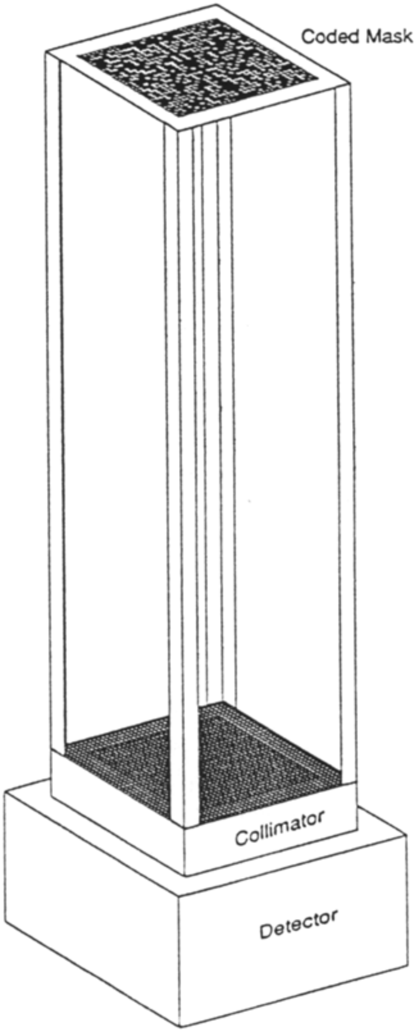

Fig. 2.8. Schematic of a coded aperture system consisting of a mask above a position-sensitive detector.

composite shadow image with the mask transmission function (Skinner, 1984).

A random array of a finite number of pinholes does not produce optimum images. This can be easily understood if one visualizes the analysis as a cross-correlation of the mask pattern with the recorded shadowgram. Moving the mask over the detector image and recording the total number of counts visible thorough the mask will result in a maximum at zero offset, but will also give other spurious peaks as groups of random holes line up with each other. To overcome this limitation a class of masks called Uniformly Redundant Arrays (URA) have been utilized (Fenimore, 1978). The defining property of this class of masks is that the distribution of separations of the pinholes is completely flat and this results in uniform sampling of all spatial frequencies. The correlation response of a URA mask is a noise-free delta function. For a fully encoded image, one or more full URA mask pattern should be visible on all parts of the detector through the field of view. For a useful aperture this means that the basic pattern is usually repeated several times in the mask so that the pattern extends to the edge of the viewing field.

The perfect mathematical response of URAs is tempered by the reality of the imperfect detectors used to encode them. Thus non-uniform backgrounds across the surface of the detectors, non-uniform absorption efficiencies, non-uniform spatial resolutions, and off-axis collimator shadowing all conspire to add unwanted artifacts to the images and must be carefully treated for optimum performance (Covault, 1991). In addition, the finite spatial resolution of the detector can smear the shadowgram, blurring the distinction between source counts and background counts. This effect has been examined by Caroli *et al.* (1987), who show that when the detector's 1σ spatial resolution approaches the mask pixel size, the signal-to-noise ratio is significantly degraded (to around 20% of the perfect detector resolution case). Ideally, the detector (FWHM) spatial resolution should over sample the mask pixels by at least a factor of two for optimum imaging ($>$80% of that for an ideal detector). Finally, motions of the instrument with respect to the source must also be removed from the data. This usually entails repositioning the raw photons in the detector on a timescale short compared with the angular resolution divided by the slew rate, or generating image maps on similar time scales and adding them after appropriate coordinate shifting.

Coded apertures have been widely used in X-ray astronomy for imaging in the energy region above that accessible to grazing incidence optics. They are capable of imaging extended objects and provide angular resolutions limited only by (1) the element size in the mask, which is set by the spatial resolution of the detector and (2) the mask-to-detector separation. For suitably large separations, 35–50 m in the case of the proposed pinhole occulter facility, imaging of a few arc sec is possible (Hudson, 1985). Coded aperture X-ray instruments have already been flown on rockets (Proctor *et al.*, 1978), balloons (Dietz *et al.*, 1992), satellites and the space shuttle (Willmore *et al.*, 1984). Typical of these is the TTM experiment that was flown on the MIR space station for imaging in the 2–25 keV energy range (Brinkman *et al.*, 1983). The instrument consisted of a position sensitive proportional counter (see Section 3.2.3), of area 25 × 25 cm, situated 1.8 m below a coded mask containing 1 mm square holes. This resulted in an angular resolution of a few arc min over a $7.5 \times 7.5°$ field of view. Similar instruments are being developed for future missions such as the MART-LIME telescope (Ubertini *et al.*, 1990) scheduled to fly on the Russian Spectrum-X-Gamma spacecraft and a proposed X-ray imager for the European INTEGRAL mission (Ubertini *et al.*, 1993).

TABLE 2.5
Characteristics of the Bragg crystal spectrometer flown on OSO-8

Energy range	1.85–8 keV
Resolving power ($E/\Delta E$)	$\lambda/\Delta\lambda = 200$ @ 2 keV, 81 @ 2.6 keV, 24 @ 6.7 keV
Effective area	$\sim 10\ \text{cm}^2$

2.2. DISPERSIVE SPECTROMETERS

2.2.1. *Bragg Crystal Spectrometers*

Developed by W. H. Bragg during the second decade of this century, a Bragg crystal spectrometer is simple in principle. X-rays of wavelength λ, when reflected off a crystal with lattice spacing d, will interfere constructively only if the angle, θ, that the incident and reflected beams make with the crystal surface satisfies Bragg's law:

$$n\lambda = 2d \sin\theta \tag{2}$$

where n is a positive integer, termed the order of the reflection. To scan a spectrum, the crystal is rotated to vary θ, and the intensity of the reflected X-ray beam is measured in a detector.

The first X-ray spectra of a celestial object, the sun, were obtained using a Bragg crystal spectrometer (Blake *et al.*, 1965). During the early 1970's Bragg crystal spectrometers were flown on three satellite missions: ANS, Ariel-5 and OSO-8 (see Table 2.5), and on occasional sounding rocket flights. Apart from the detection of a 6.8 keV iron line from Cyg X-3 (Kestenbaum *et al.*, 1977) and of oxygen emission at 0.65 keV from supernova Puppis A (Zarnecki and Culhane, 1977), these early attempts to obtain X-ray spectra from extra-solar sources were largely unsuccessful due to low signal-to-noise ratios. {All but the strongest X-ray sources have line fluxes $\leq 10^{-3}$ photons $\text{cm}^{-2}\text{s}^{-1}$}. Bragg crystal spectrometers generally have peak efficiencies which lie below 10% and an irreducible induced background rate of $\sim 10^{-3}$ events $\text{cm}^{-2}\ \text{s}^{-1}\ \text{keV}^{-1}$ (Markert *et al.*, 1988). Hence, to study the spectra of any but the most powerful X-ray sources, a Bragg crystal spectrometer requires that the effective area be made greater than the detector area either by curving the crystal to focus the reflected X-rays or by using the spectrometer in conjunction with an X-ray concentrator.

X-ray spectroscopy came of age with the launch of the Einstein observatory in 1978. The Einstein Focal Plane Crystal Spectrometer (FPCS) consisted of a curved graphite crystal placed outside the focus of the grazing incidence mirrors (Figure 2.9(a)). Useful spectra were possible because the FPCS was able to concentrate the signal to a significant degree. The curvature of the crystal served to maintain a nearly constant Bragg angle for the incident, diverging beam, and to refocus the beam onto an imaging proportional counter. Since the proportional counter was able to distinguish position with an accuracy of 0.5 mm, the detector was equivalent

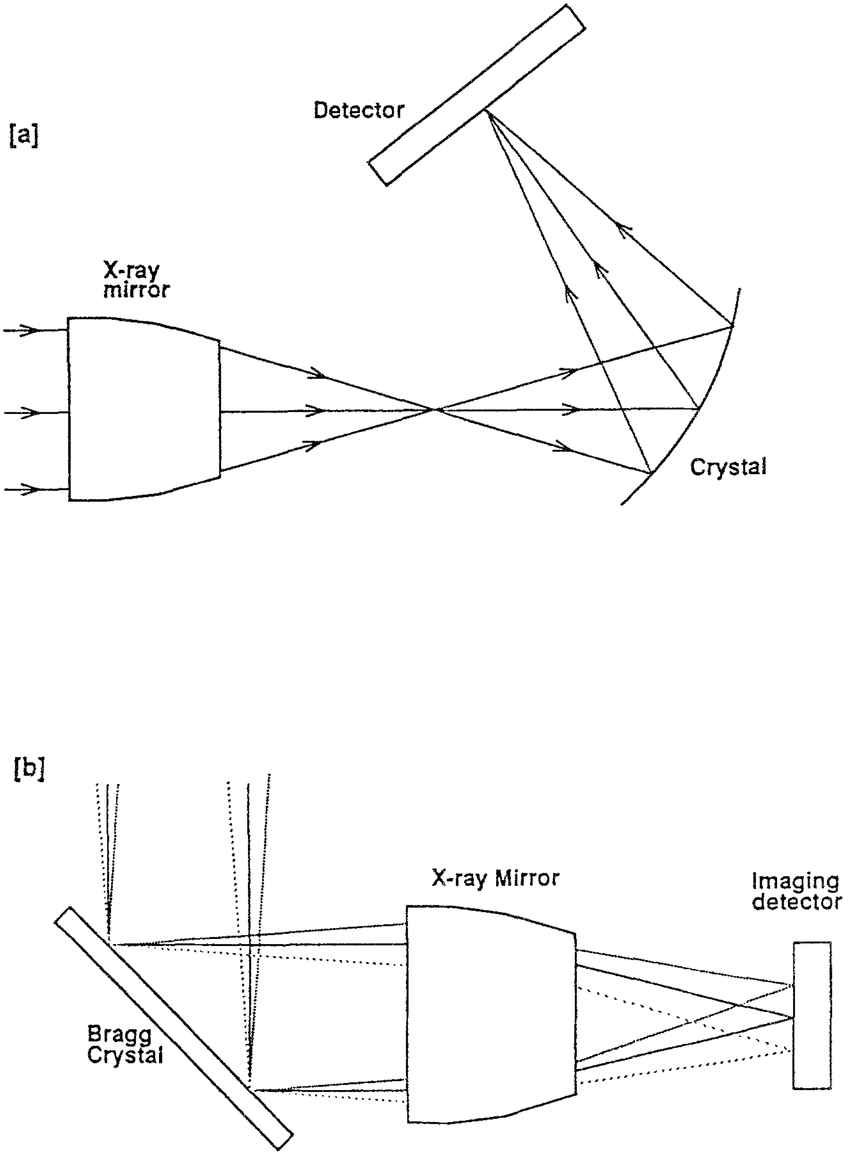

Fig. 2.9. Two configurations for a Bragg crystal spectrometer: (a) a Focal Plane Crystal Spectrometer (FPCS) and (b) an Objective Crystal Spectrometer (OCS) – see text for details.

to a non-imaging detector with size comparable to the focused spot. To scan an X-ray spectral feature, the FPCS and imaging detector positions were adjusted to scan through a range of Bragg angles; by correlating the measured intensity of the reflected beam with the Bragg angle, an X-ray spectrum was built up.

Another configuration that has been considered for a Bragg crystal spectrometer is the objective crystal spectrometer (OCS). An OCS has been proposed for the

European XMM mission. This configuration consists of a flat Bragg crystal in front of an X-ray telescope as in Figure 2.9(b). X-rays incident on the crystal are scattered into the telescope aperture and are then focused onto an imaging detector. By scanning the crystal panel or telescope-detector combination over an extended source, different parts of the source will satisfy Bragg's law. By recording the orientation of the crystal-telescope combination as a function of time, an X-ray image as a function of energy can be reconstructed. The ability to maintain high spectral resolving powers for extended sources is a significant advantage over transmission gratings (described below) which work best for point sources lying on the optical axis of the telescope. Another attractive feature is that a telescope need not have extremely high resolving power for this technique to work effectively. An OCS can perform spectral imaging over a field of view as large as the effective field of the telescope; for XMM the effective field will be 30 arc min.

2.2.2. *Transmission Spectrometers*

With the advent of high-quality grazing incidence mirrors having angular resolutions of around 1 arc sec or better, transmission gratings have become the favored spectrometers for X-ray astronomy. A grating with N bars has a theoretical resolution at first order of λ/N. When passed through a transmission grating with a grating period p, X-rays having wavelength λ, will have interference maxima at angles θ, obtained from: $n\lambda = p\sin\theta$, where n is an integer. Because of the small dispersion possible with reasonable grating periods (~100 nm), even the best currently available X-ray mirrors limit the resolving power of the grating when N becomes larger than ~1000. To obtain large areas, a grating can be made up of an array of small gratings (facets). Alignment tolerances between individual gratings need not be very stringent, and a large grating can be built up from many facets without undue difficulty (Gursky and Zehnpfennig, 1966). Transmission gratings work optimally for observing point sources, their resolution being poorer for extended sources since off-axis rays will cause broadening of the dispersion spectrum. Some problems to be dealt with when employing transmission gratings are: a uniform background of scattered X-rays from the gratings, and dispersed photons from off axis sources, both of which will make it more difficult to analyze results. As is always the case, sensitivity will also be affected by the background (intrinsic, environmental, and cosmic) coming from the detector.

The first transmission gratings used to obtain extra-solar X-ray spectra were flown on the Einstein and the European EXOSAT missions. The gratings for both experiments used facets that were replicated from holographically produced masters. Although EXOSAT had higher-quality gratings than those on Einstein, the lifetime of the gratings was prematurely cut short due to an early failure of the grating insertion mechanism. The facets for the Einstein grating spectrometer were formed by exposing a sandwich of photoresist, nickel, and glass to the interference pattern produced by a laser beam that had been split into two beams and then recombined. By then etching and plating with gold, bar thicknesses of 0.2 μm were

TABLE 2.6
A summary of Einstein OGS parameters

Energy range	0.2–2.0 keV
Resolving power ($E/\Delta E$)	$\lambda/\Delta\lambda \approx 50$ @ 1 keV (point-source)
Effective area	$\sim$1 cm^2
Grating period	2000 nm and 1000 nm
Imager	HRI

achieved (Schnopper *et al.*, 1977). Two sets of grating facets with grating periods of 1000 nm and 2000 nm were assembled into the complete OGS (see Table 2.6). The OGS (Seward *et al.*, 1982) was used for energies below 1.5 keV, since for higher energies, the Solid State Spectrometer (SSS) performed better (see Section 3.4.4). Using the OGS, the first X-ray absorption feature (due to ionized oxygen) from an extra galactic source, BL lacertae object PKS 2155–304, was detected at $\sim$600 eV (Canizares and Kruper, 1984).

The transmission gratings that will be flown on the AXAF-I mission define the current state of the art for this type of X-ray spectrometer. AXAF-I will have two separate grating spectrometers covering two overlapping energy ranges: the Low Energy Transmission Grating (LETG) and the High Energy Transmission Grating (HETG). The two gratings will have similar configurations with numerous grating facets mounted on a plate machined to conform to the surface of a Rowland torus – the surface chosen to minimize optical aberrations (Samson, 1967). To maximize spectral resolution, the X-ray detector for each spectrometer will be segmented in order to approximate the curvature of the Rowland torus. Grating facets will be mounted on four concentric rings which correspond to the four mirror pairs.

The LETG, which is being developed at the Laboratory for Space Research in Utrecht, The Netherlands, in collaboration with the Max-Planck-Institut für Extraterrestrische Physik in Garching, Germany, will provide the highest spectral resolution on AXAF at low X-ray energies (0.09–3 keV). The $\sim$ 150 grating facets will be produced by a technique that is similar to that used to make the gratings for EXOSAT. The grating bars are 0.5 μm wide, 0.4–0.45 μm thick, and will have a spacing of 0.5 μm. The bar thickness was selected to suppress transmission in even spectral orders (phased). The HRC-S microchannel plate detector is the baseline focal plane detector for the LETG. Order discrimination will not be possible due to the poor energy resolution of the HRC-S detector; instead, part of the HRC-S will be coated with a thin layer (20 nm) of aluminum to allow discrimination between 1st and 2nd order diffraction by comparing spectra that have been dispersed onto the coated areas with those that have been dispersed onto the uncoated areas (see Table 2.7).

The HETG is being developed at the Massachusetts Institute of Technology. This grating will have an energy resolution ($E/\Delta E$) up to 1000 between 0.4 and

TABLE 2.7
A Summary of LETG parameters

Energy range	0.09–3.0 keV
Resolving power (E/ΔE)	$\lambda/\Delta\lambda \approx 20\lambda$ (point-source)
Effective area	~ 20 cm^2
Grating period	1000 nm
Imager	HRC (microchannel plate)

TABLE 2.8
A summary of HETG parameters

Energy range	0.4–10.0 keV
Resolving power ($E/\Delta E$)	60–1000 (point-source)
Effective area	up to 100 cm^2
HEG period	200 nm
MEG period	400 nm

10.0 keV. The ACIS-S CCD is intended to be the focal plane detector. Order overlap and source confusion can be sorted out by utilizing the intrinsic energy resolution of the ACIS CCD detector. As with the LETG, grating bar thicknesses have been chosen to suppress zero-order intensities (phasing) in order to strengthen first order dispersion through conservation of energy (Schattenburg *et al.*, 1988) (see Table 2.8). The HETG will be comprised of 336 grating facets which will be grouped into two sub-gratings; one, the Medium Energy Grating (MEG), will cover the outer two mirror shells and will be optimized for operation at $\sim$2 keV; the other, the High Energy Grating (HEG) will cover the inner two mirror shells and will be optimized for operation at $\sim$6 keV. The HEG and MEG will be mounted with their rulings at different angles so that their dispersed images will form a shallow X centered on the undispersed position (Figure 2.10).

2.3. POLARIMETERS

The measurement of polarization presents a special challenge in X-ray astronomy. In addition to the usual problems of low source flux and high backgrounds, a measurement of say 10% polarization in a source must be performed against a 90% unpolarized component. Thus the nature of the signal coupled with the low efficiencies of polarimeters in general, conspire to make this a difficult area of study.

2.3.1. Bragg Crystal Polarimeters

To date, most polarimeters utilize either Bragg reflection or Compton scattering of the incident photon to measure polarization. Bragg reflection takes place from a

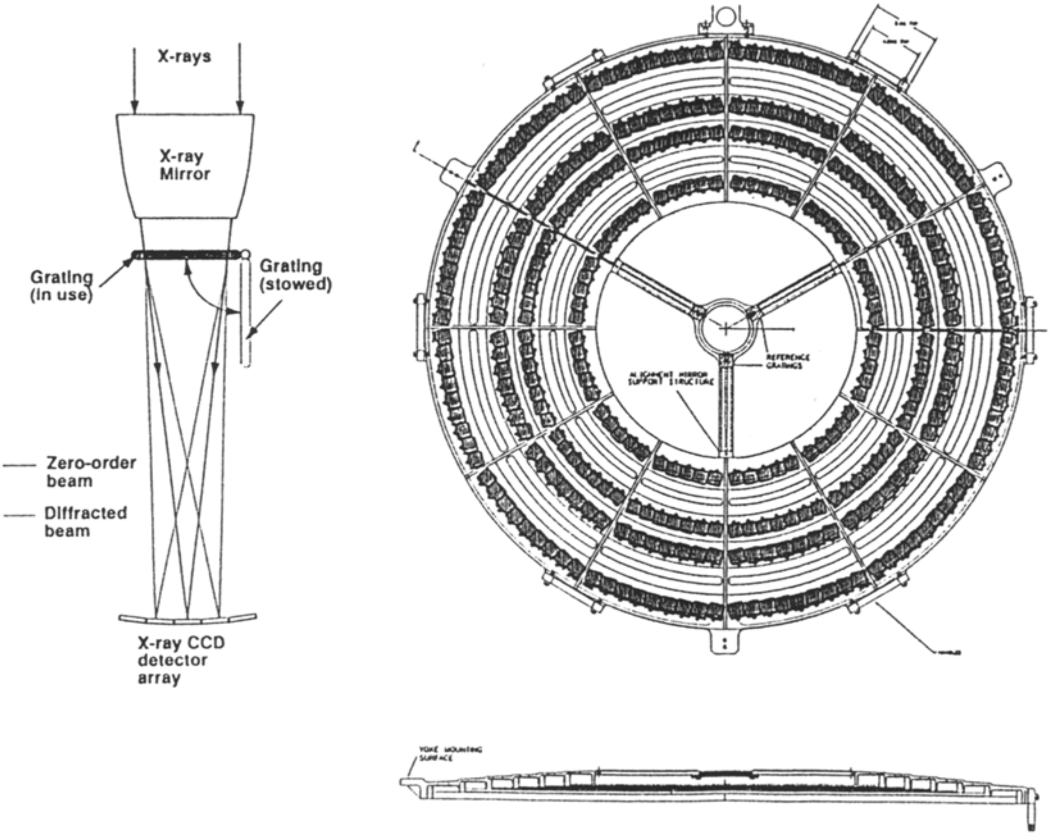

Fig. 2.10. Proposed configuration for the high energy transmission gratings on AXAF. Figure left shows the location of the gratings in the beam line and figure right details the proposed arrangement of the grating facets.

crystal surface when the well known Bragg condition (see Section 2.2.1) is met. The radiation satisfying this condition has maximum reflectivity when its electric field vector is parallel to the crystal planes but zero reflectivity when the field is normal to the planes. Thus polarized X-rays will be reflected only for certain orientations of the crystal; and so, if a crystal is used to scatter X-rays through 90° and is then rotated around the line of sight, the reflected signal will be modulated, sinusoidally, at twice the rotation frequency. This is the basis of Bragg crystal polarimeters.

A figure of merit for all polarimeters is the modulation factor μ which is defined as the ratio of the amplitude of the sinusoidal modulation for 100% polarized X-rays to the average count rate in the absence of background. This can be used to derive a sensitivity from the equation:

$$\mathrm{MDP} = (429/\mu R)((R+B)/T)^{0.5}\,, \tag{3}$$

where MDP is the minimum detectable polarization (%) at the 99% confidence level, R is the source count rate, B is the background rate and T is the integration time (Elsner *et al.*, 1990). As the modulation factor is outside of the square root then for an efficient polarimeter it is of prime importance to keep this value as high as possible. The Bragg polarimeter can achieve very high modulation factors (above 0.99) but its main drawback lies in the fact that it operates only at specific energies that satisfy the Bragg condition. For a graphite crystal, as was used on a polarimeter aboard the OSO-8 satellite, these are centered on 2.6 and 5.2 keV for the first and second order reflections. Beyond the second order the reflected intensity becomes too weak to be useful. The OSO-8 polarimeter produced the only unambiguous measurement to date of polarization of a cosmic source; that of 19% linear polarization from the Crab Nebula (Weisskopf *et al.*, 1978). A Bragg crystal polarimeter utilizing graphite is being developed as part of the Stellar X-ray Polarimeter experiment (SXRP) on board the Spectrum-X-Gamma mission planned for launch in 1996. Figure 2.11 depicts the SXRP instrument which also contains a Compton Scattering Polarimeter (Kaaret *et al.*, 1993).

2.3.2. *Compton Scattering Polarimeters*

A Compton scattering polarimeter makes use of the fact that when photons Compton scatter, their angular distribution is peaked in the direction normal to the plane containing both the momentum vector and the electric vector of the incident X-ray beam. If a suitable low atomic number scatterer is used and surrounded on all sides by X-ray detectors, then the angular distribution of detected events can be used to derive the polarization of the incident flux. Low-Z materials are the most attractive as they maximize the Compton scattering cross section relative to photoelectric cross section, reducing the likelihood of the scattered photon being absorbed before it exits the scatterer. Compton scattering polarimeters can achieve high modulation factors: an instrument being developed as the second half of the SXRP package (see Figure 2.11) will utilize a lithium scattering block and will have a modulation factor of 0.77 at 6 keV and 0.71 at 20 keV (Kaaret *et al.*, 1993). However, typical of this type of instrument, the overall efficiency is quite low, with only a few percent of the photons hitting the scatterer being registered in the surrounding detectors. The size of the scattering block must necessarily be kept small to reduce the probability of additional scatters or of absorption, and to reduce solid angle effects for photons far from the axis of the system which could give rise to additional signal modulations. Hence the Compton scattering polarimeter is ideally suited to low energies where grazing incidence optics can be used to focus the source flux to a small region, as in SXRP. At higher energies, in order to achieve large collecting areas it is necessary to either have one large, thin, scatterer and accept lower efficiencies and modulation factors or to assemble multiple scattering units which can quickly become unwieldy. It is interesting to note that once the *gamma-ray* region is reached, and Compton scattering dominates, the scatterer and detector can be one and the same. Such is the case in the proposed INTEGRAL imaging detector where multiple detector elements permit reconstruction of the scattering history of incident photons (Swinyard *et al.*, 1991).

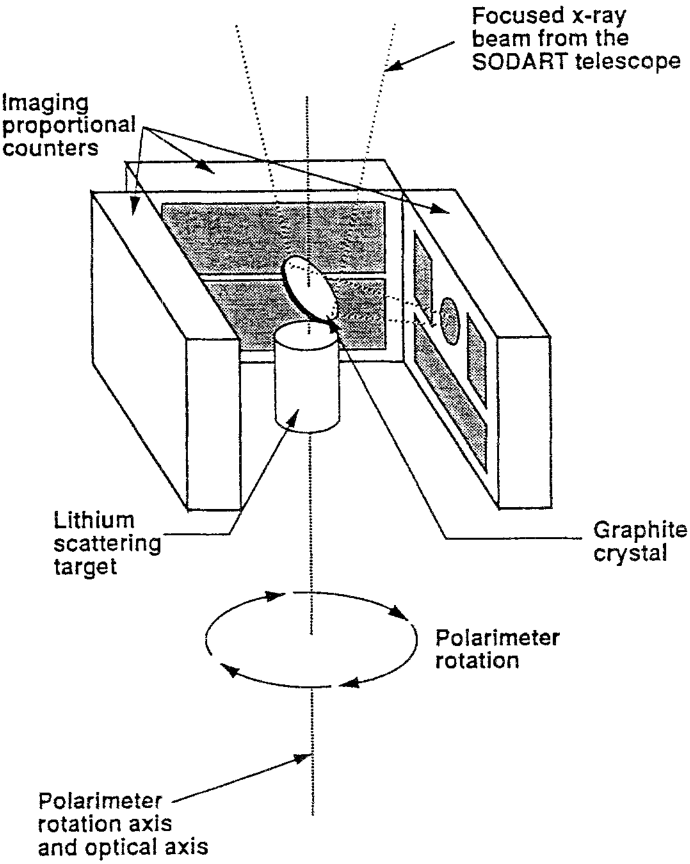

Fig. 2.11. A schematic of the Stellar X-Ray Polarimeter (SXRP) scheduled to fly on the Spectrum-X-Gamma mission. The instrument contains both Bragg (graphite crystal) and Compton scattering (lithium target) polarimeters.

2.3.3. Photoelectric Polarimeters

A different approach for higher X-ray energies makes use of the angular dependence of the emitted photoelectron on the polarization of the absorbed X-ray photon. In photoelectric interactions, a K shell electron is ejected from an atom with an angular distribution given by

$$\mathrm{d}n/\mathrm{d}\Omega \propto \sin^2\theta\cos^2\phi/(1-\beta\cos\theta)^4\,, \tag{4}$$

where θ is the radial angle between the incident photon direction and the ejection direction of the photoelectron, ϕ is the azimuthal angle between the electric vector of the incident photon and the ejection direction of the photoelectron and β is the magnitude of the electron's velocity divided by the speed of light. From this it is seen that a photoelectron is preferentially emitted in the direction of the electric field vector of the incident photon. A novel technique to exploit this phenomenon utilizes an intensified CCD camera to image photoelectron tracks in a proportional counter containing a special ultraviolet emitting vapor (Austin and Ramsey, 1993). By determining the origin of the track and then measuring the initial photoelectron's ejection angle, a measure of the degree of polarization of the source photons is derived. This technique appears to work best at moderately high energies (30–70 keV) where the electron track length is long and the initial portion of the track is relatively free from large angle scatters which would mask the true emission direction. Such an instrument is currently being developed for X-ray astronomy from high-altitude balloons (Austin *et al.*, 1993).

2.4. BACKGROUNDS AND SHIELDING

The weak photon flux from celestial X-ray sources has to compete with the ever-present radiation background at the detector. The ratio of source photons to this background (signal-to-noise ratio, S/N) is a major factor in determining the minimum detectable flux from a source. Typically, for non-focusing systems, observations in X-ray astronomy are background limited, where the size of the background flux determines the minimum detectable source flux. For focusing systems, where the source flux is concentrated into a small detector area, a very large increase in the S/N ratio is possible and many observations are photon limited, i.e., limited by the small number of source photons registered.

Several components contribute to the background for instruments at balloon or satellite altitudes (Gehrels, 1985, 1992). There is a diffuse, isotropic X-ray and gamma ray background across most of the spectrum. This manifests itself mainly as an aperture flux, dependent upon the field of view of the instrument, but can also give rise to an indirect background component through shield penetration. A second component is primary cosmic rays (mostly protons) and trapped particles in the Earth's radiation belts. These interact with the detector and can mimic the absorption of real photons. They can also produce prompt and delayed secondary photons through interactions with the detector or the spacecraft structure and, in addition, they act on the Earth's atmosphere producing a large atmospheric gamma ray component. The interaction of cosmic rays also produces a secondary neutron flux which can either elastically scatter in the detector, giving rise to prompt background counts, or induce radioactivity in the structure of the detector and the spacecraft which in turn gives rise to background photons. Finally, there may also be natural radioactivity in the materials used for the construction of the instrument.

As the Earth's magnetic field shields against the lower energy particles, the lowest backgrounds can be achieved in low-inclination, low-altitude orbits. Frequently, though, equatorial orbits are impractical due to the latitude of the launch site, and highly eccentric orbits are often chosen to increase the available continuous observing time of sources. Thus the instruments must be shielded as efficiently as possible, and other techniques must be employed to reduce the residual background.

Radiation which enters the detector from the sides and from the rear can be eliminated or reduced by enclosing the detector (except for the window) in a high atomic number shield which absorbs the unwanted radiation (passive shielding).

Passive shielding against high-energy radiation requires heavy shields which are undesirable for space-borne detectors. A more efficient technique is active shielding which uses one or several additional detectors surrounding the primary detector. With proper geometrical arrangement of the secondary or shield detector, radiation from outside the field of view would have to penetrate both the shield and the primary detector causing simultaneous outputs from both detectors. An electronic anticoincidence circuit prevents the counting of events yielding these simultaneous responses (anticoincidence shield). Charged particles (e.g., cosmic rays) entering through the detector window can be discriminated against by using a secondary detector with a low absorption cross section for photons in front of the primary detector. Charged particles interact with both detectors causing simultaneous output signals which are then rejected, while the photons interact only with the higher cross section primary detector and are counted as true events.

In some cases it is possible to reject events on the basis of their signature. High-energy charged particles leave a trail of ionization, whereas photons tend to interact at a single point. Thus by looking for highly elongated tracks, which may manifest themselves as events with extended positions in imaging detectors, or as events having long signal risetimes in the case of, say, gas-filled detectors, the charged particles can be discriminated against. In addition, high-energy charged particles have a much lower rate of energy deposition than low-energy photo-electrons, and so additional charged particle discrimination can be performed on the basis of ionization density within the event.

Background rejection is of paramount importance in large-area detectors working at high energies where focusing cannot be employed. Typically, these detectors are gas filled counters which employ the techniques described above, but in addition can make use of the phenomenon of fluorescence gating (Ramsey *et al.*, 1990). Here, use is made of the fact that photons interacting in the detector gas cause fluorescence of the gas and the resulting fluorescent photon, which is also in the X-ray region, can then be absorbed elsewhere in the detector. This results in a pair of separate, though correlated events, which is the mark of a true X-ray interaction. High energy photons, which Compton scatter in the gas, have a very low probability of producing fluorescence, as do charged particles (Dietz *et al.*, 1993). Thus the technique is a powerful additional means of background reduction.

As well as shielding and residual rejection techniques, further benefits can be derived from careful choices in the materials used in the detector construction. This includes the following: utilizing materials with low natural radioactivity, picking detector body materials which prevent down scattering of high-energy photons into the sensitive energy range (Bower *et al.*, 1991), and employing materials which have a low cross section for neutron or charged particle activation. A good example of the latter is the choice of isotopically enriched germanium which has a low cross section for neutron activation compared with naturally occuring germanium. This results in a factor of two reduction in residual background in these semiconductor detectors (Gehrels, 1992a).

Finally, another aspect of background shielding involves the prevention of physical damage to the detector and its electronics. This can range from the build-up of deposits in gas-filled detectors to damage of the pixels in CCD detectors. It is a major concern for long duration missions and necessitates the use of radiation hardened electronics, additional instrument shielding, favorable orbits, and procedures for reversing the damage, such as annealing at elevated temperatures.

3. Detectors

3.1. BASIC PRINCIPLES

An X-ray photon interacting with the detector medium ultimately liberates charges, and these provide the means to measure the event. In some detectors, the charged particles are collected directly to generate an electrical signal at the output of the detector. In a gas scintillation detector the charged particles produced by the incident photon generate, through secondary interactions, a light pulse which is converted by a photomultiplier into an electrical signal. In a calorimeter detector the absorbed energy of the incident photon causes a small temperature increase of the absorber material, and this temperature change is converted, via a thermometer, into an electrical signal. Regardless of the detector type, *each* photon interaction generates a *discrete* electrical signal which is amplified and processed by the detector electronics to obtain information about the properties of the incident radiation (intensity, energy, arrival time, etc.).

The amplitude of the electrical pulse signal at the detector output is usually a measure of the incident X-ray photon energy. To determine the energy distribution (spectrum) of the received radiation, the pulse signals are sorted in bins according to their amplitude with each bin representing a small energy interval. The energy spectrum of the source can then be reconstructed from this pulse height spectrum by taking out the spectral response of the instrument which is itself derived from careful calibration.

The energy resolution of a detector is defined as its response to monoenergetic radiation. Typically, the shape of the detector response approximates a Gaussian distribution centered on the line energy input. The Full Width Half Maximum (FWHM) energy resolution is defined as the distribution width, ΔE, at half maximum peak height divided by the input energy, E, and is usually expressed in percent for a given energy. It determines the detector's ability to resolve details in the energy spectrum of the source, for example to separate adjacent spectral lines. Spectroscopic detectors are optimized for high energy resolution, and some can achieve a resolution of less than 1%.

The energy resolution of a detector depends on various parameters including the type and design of the detector, the interaction process and sources of random noise in the detector, and the signal electronics. Accurate measurement of the incident photon energy requires that the photon deposit all its energy in the detector absorber; i.e., the primary photon and the secondary interaction products (electrons, photons) must be stopped completely in the absorber. Even in a large high-Z detector there are always events in which only a portion of the primary photon energy is deposited in the absorber and these contribute to the uncertainty in the energy measurement. (For example, in Compton interactions and interactions near the surface or edge of a detector the primary photon or some secondary photons or electrons may escape from the absorber.) Another source of uncertainty in the energy measurement, which applies to all types of detectors and which is always present, is the statistical noise connected with the discrete number of information carriers generated in the interaction event. For example, in a gas-filled counter the photon energy is converted into a number of electron-ion pairs, and in a gas-scintillation counter the primary photon energy is converted into a number of ultraviolet photons. If the creation of information carriers were a series of completely independent events, Poisson statistics would apply and the standard deviation would be just the square root of the total number of carriers produced. In this case the FWHM energy resolution would then be 2.35 times the standard deviation. Because the creation of information carriers is not a series of completely independent events, the statistics of this process is usually found to produce better resolution than would be predicted from Poisson statistics and the Fano factor, F, was introduced to quantify this deviation. The energy resolution is now given by

$$\Delta E/E(\%\mathrm{FWHM}) = 2.35(F/N)^{0.5} \times 100\,, \tag{1}$$

where N is the number of primary information carriers produced. F typically has a value of less than 1 for gas-filled and semiconductor detectors.

1.1. GAS-FILLED DETECTORS

1.1.1. Introduction

Gas-filled detectors function by detecting the charge liberated when a photon interacts with the fill medium. In the energy range where these detectors are normally employed this interaction is predominantly the photoelectric effect and the charge is liberated through ionizing collisions as the initial photoelectron, and de-excitation products, come to rest in the detector gas. The number of free electrons produced is proportional to the absorbed photon's energy and is dependent on the characteristics of the fill gas. Typically, a mean energy of 20–25 eV is needed to produce an electron-ion pair, so that a 20-keV incident photon would produce around 1000 electrons. As the Fano factor for commonly-used detector gases is in the range 0.2–0.3, the Fano limiting resolution for gas-filled detectors would be 3–4% FWHM at 20 keV, *were there no other contributing factors.*

There are many different types of gas-filled detectors. Ionization chambers simply register the initial ionization produced but are not really useful for X-rays because at the energies where gas-filled detectors are efficient, typically below 100 keV, the signals are too small to drive processing electronics. Proportional counters and gas scintillation proportional counters internally amplify the signal to useful levels, even for very low-energy photons and, hence, have found widespread

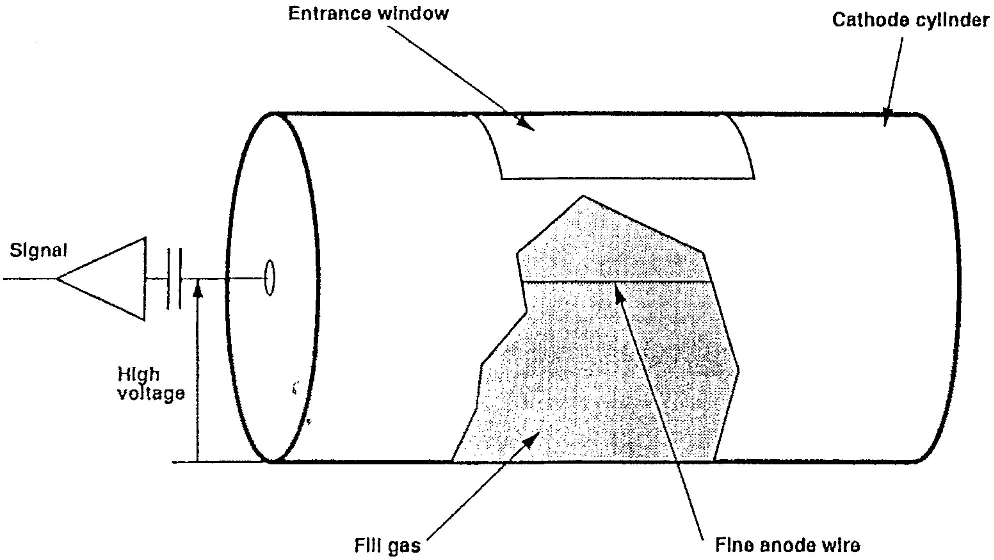

Fig. 3.1. The features of a single wire proportional counter.

use in astronomy. Geiger counters produce very large saturated pulses when irradiated but have no energy information and, as a consequence, are not used directly in this application, but a derivative of this device, the spark chamber, is sometimes used for high-energy photon detection (MeV range).

3.2.2. *Proportional Counters*

Proportional counters rely on the phenomenon of gas multiplication to amplify the signal from the tiny primary electron cloud, typically containing 10^3 electrons for a 20-keV absorbed photon, to the 10^5–10^7 electrons necessary for driving preamplifiers and processing electronics. The device came of age in the late 1940s, early 1950s (Wilkinson, 1950), and has since developed into a highly sophisticated instrument for use in such areas as high-energy physics from which the bulk of the later development work has come (Charpak *et al.*, 1968)

In its simplest form, as shown in Figure 3.1, the proportional counter consists of a single fine wire, the anode, concentric with a gas-filled cylinder which forms the cathode. A positive high potential (V), relative to the cathode, is applied to the anode, and electrons liberated in the gas by absorbed photons drift toward the central wire. The field E at a distance r from the anode center is given by

$$E(r) = V/(r \ln(b/a)) , \tag{6}$$

where b is the cathode inner radius and a is the anode radius. The field therefore increases as the wire is approached. At a distance of a few wire radii from the wire surface, where the field is typically $>10^5 \mathrm{V\ cm^{-1}}$, the drifting primary electrons gain enough kinetic energy from the electric field to ionize the fill gas and produce secondary electrons which, in turn, have further ionizing collisions. In this way an avalanche is produced close to the anode wire surface in which each primary electron produces a large, but roughly constant, number of secondaries. Gas multiplication factors, usually termed gas gain, of $>10^4$ are typically possible before saturation sets in, at which point the charge in the leading edge of the avalanche becomes so great that the local electric field is distorted and non-linearities in response occur. The gain is dependent on the applied voltage, the detector geometry, and the fill gas. Typical proportional counters would have a 25 μm diameter anode, an anode-cathode distance of 1–2 cm, and would be filled to a pressure of 1 atm. A thin entrance window would permit X-rays to enter the chamber. They are not restricted solely to this coaxial configuration and are sometimes used with other geometries such as the parallel field case where charge multiplication takes place between pairs of mesh grids (Charpak *et al.*, 1989) The term proportional counter is used in all cases as the output signal size remains proportional to the input photon energy. The fact that the avalanche region is very close to the wire for the coaxial geometry ensures that each electron cloud experiences the same multiplication factor regardless of where the original photon is absorbed in the detector.

The signals from a proportional counter typically have very fast initial rise times, less than 1 μs, due to the high velocity of the charges in the intense field near the wire. The bulk of the signal is in fact induced by the motion of the positive ions away from the anode as these move through a much greater potential difference than the electrons. These ions move very rapidly at first but then slow down as regions of weaker field are reached away from the anode. The total collection time for the ions can be $\approx$100 μs but the signal is normally shaped with a short electronic time constant so that only the initial fast rise time is seen by the processing electronics.

The choice of fill gas is determined by the application. Noble gases are usually chosen over complex polyatomic molecules as the latter have many rotational and vibrational energy levels which can waste energy that could otherwise have gone into ionization. Under most circumstances, however, pure noble gases alone do not operate stably at moderate to high gas gains due to the emission of ultraviolet photons in the avalanche. These photons can cause ionization in the walls of the detector and the resulting free electrons can drift to the wire and produce serious after pulses. To prevent this, a small quantity, usually a few percent, of a polyatomic quench gas is added to provide stable operation either by direct absorption of the photons or through de-excitation of the noble gas atoms before ultraviolet emission occurs. Typical fill gases in X-ray astronomy are argon and xenon with carbon dioxide or methane as quench additives. Xenon ($Z = 54$) is preferable to argon ($Z = 18$) at energies above 10–20 keV as the photoelectric cross section scales as Z^n, where n is between 4 and 5. Even so, xenon quickly becomes transparent at higher energies so that with few exceptions, proportional counters are rarely used above 100 keV.

The choice of quench gas can also affect the performance of the counter. Pure noble gases have low electron drift velocities and are very susceptible to electronegative contaminants which can remove electrons from the drifting primary charge cloud. The addition of a small percentage of methane can speed up the drift by more than a factor of 10 and render the counter relatively insensitive to contaminants which outgas from the detector walls and interior components. For long lifetime applications another consideration is the buildup of deposits on the anode wire through the gradual polymerization of the quench gas. This detector aging is most noticeable in methane-quenched detectors yet appears not to occur when carbon dioxide is used; consequently, this latter quench gas has been widely used in satellite applications (Ramsey and Agrawal, 1988).

More exotic quench gases can be utilized to improve the performance of the standard proportional counter. The so-called Penning gas mixtures are ones in which the quench gas is specifically chosen to collisionally de-excite long-lived states in the noble gas resulting in subsequent ionization of the quench additive. This increase in ionization improves the energy resolution of the detector and reduces the high voltage requirements (Ramsey and Agrawal, 1989).

The energy resolution of a proportional counter consists of two components. The first is governed by the statistics of the initial photo-ionization process and the second comes about from the charge multiplication process. The standard formula for this resolution at energy E is

$$\Delta E/E(\%\text{FWHM}) = 2.35((W(F+A))/E)^{0.5} \times 100\,, \tag{7}$$

where W is the mean energy to form an electron-ion pair, F is the Fano factor (see Section 3.1), and A is the relative variance of the multiplication factor for a single electron. The multiplication variation comes about from small changes in the relative amounts of energy going into excitation versus ionization in the first few steps of the avalanche and results in corresponding changes in the amplification factor from event to event. This component is by far the larger of the two and dominates the energy resolution of practical proportional counters. Typical values are around 0.2 for F, 0.6 for A, and $W = 26$ eV for argon+methane, resulting in an energy resolution of around 14% at 5.9 keV for a single wire detector. Despite much work with special gas mixtures and different geometries, it has proven very difficult to improve on this value.

3.2.3. Multiwire Proportional Counters

To satisfy the desire for large collecting areas and position sensitivity, the Multiwire Proportional Counter (MWPC) was developed (Charpak *et al.*, 1968). This device, shown schematically in Figure 3.2, consists of planes of anode wires sandwiched between planes of cathode wires to form a series of cells, each of which can be looked on as a single wall-less proportional counter. The full sensitive volume of the detector can either be filled with these cells, Figure 3.2(a), as was the case with the monitor proportional counters on the Einstein satellite (Gaillardetz *et al.*, 1978), the large area counters on the GINGA satellite (Table 3.1 and Figure 3.3), and the proposed proportional counter array for the X-Ray Timing Explorer (XTE) (Bradt

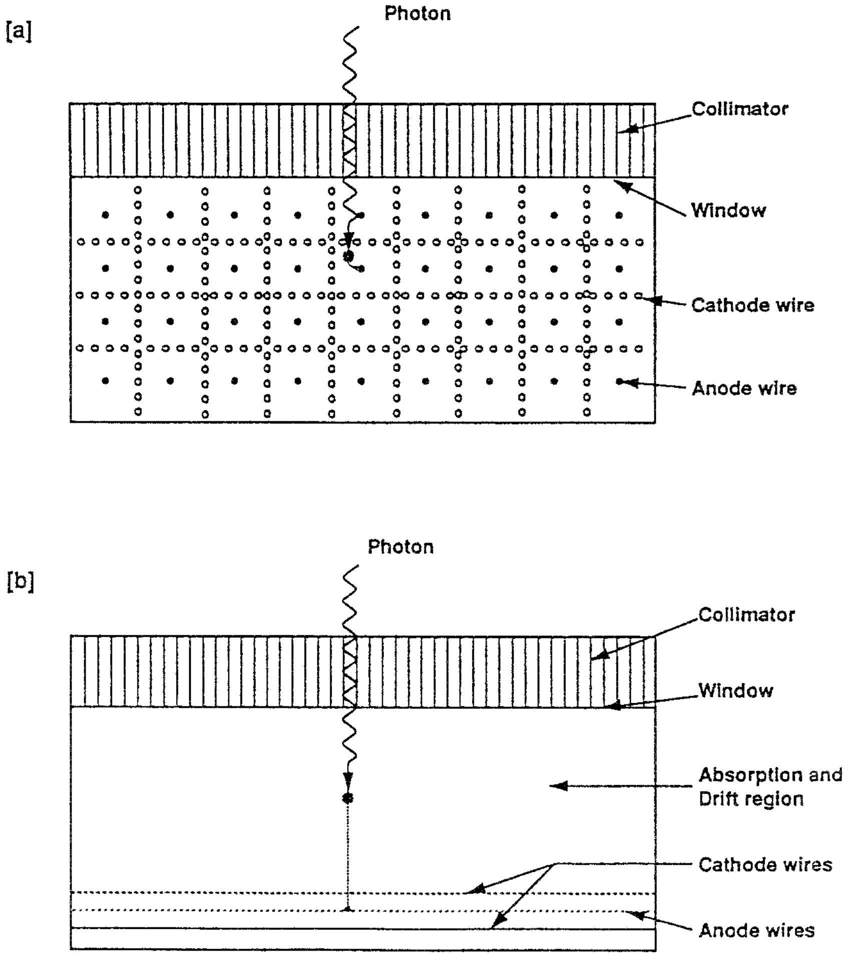

Fig. 3.2. Different approaches to Multiwire Proportional Counter (MWPC) design. In (a) the sensitive volume is filled with individual cells, while in (b) there is a large absorption and drift region followed by a single, thin, multiwire sensing region.

et al., 1990), or there can be an absorption and drift region followed by a sense region, as shown in Figures 3.2(b) and 3.4. The latter configuration is typically used if position sensing is required, as is the case when the detector is at the focus of an X-ray reflecting telescope or in a coded aperture system.

The front end of the MWPC often has a collimator designed both to define a region of the sky from which to accept X-rays and to support the thin entrance window which permits X-rays to enter the detector. Sometimes the collimator is omitted, as at the focus of telescopes, and a mesh provides window support. For low-energy applications, below a few keV, these windows are normally made from thin plastics (down to 1 μm) coated with carbon or aluminum to make them conducting and prevent charge from building up on their inner surface. At higher

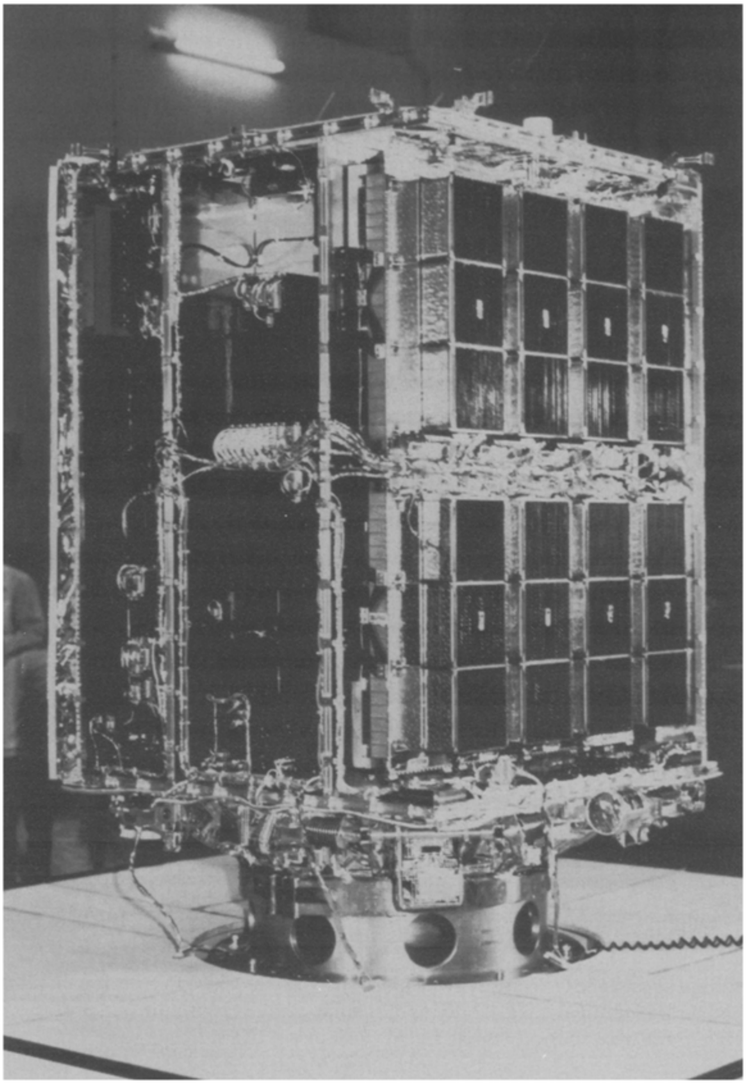

Fig. 3.3. The large-area proportional counters on board the GINGA spacecraft (courtesy of the University of Leicester).

energies, beryllium or even aluminum foils or sheets can be used and these can be quite ‘thick’. For balloon-borne detectors, where the residual atmosphere cuts off the low-energy flux below 20 keV, aluminum windows as thick as several hundred microns can be utilized without loss of signal.

Many applications, for example in X-ray telescopes, demand that the MWPC be position sensitive and there exists a multitude of schemes for deriving the position of events within the counter. These usually rely on induced signals in the mutually orthogonal top and bottom cathode planes. By connecting the cathode wires, either

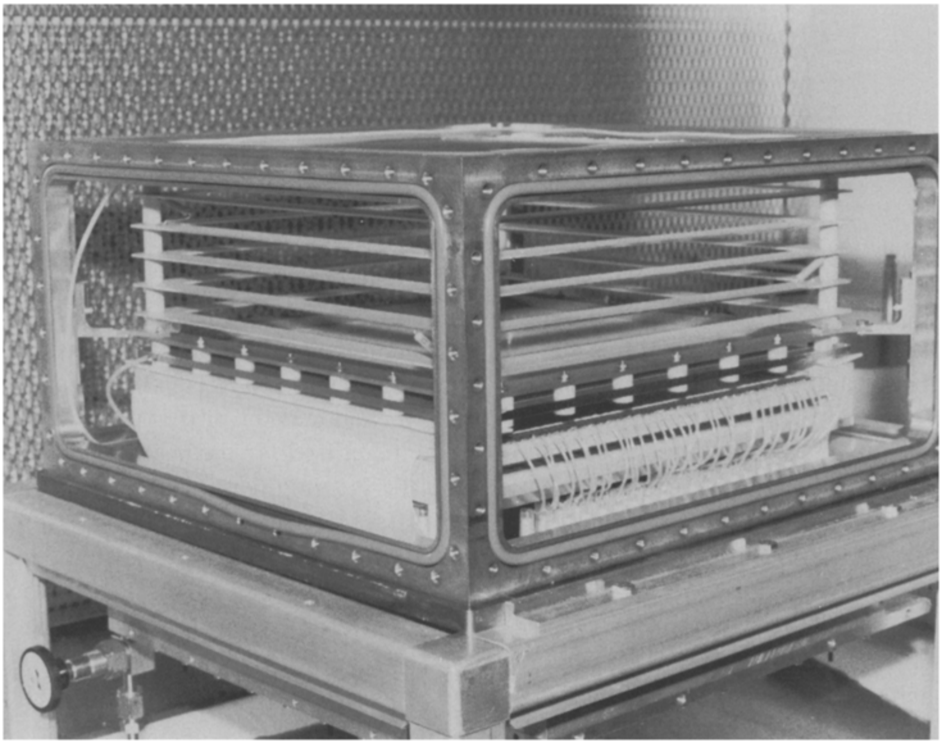

Fig. 3.4. The interior of a large-area imaging proportional counter with drift volume constructed at the Marshall Space Flight Center.

TABLE 3.1
Characteristics of the GINGA large-area counter (from Turner *et al.*, 1989)

Sensitive area	4000 cm^2 (eight detectors)
Window	62 μm beryllium
Fill gas	75% argon + 20% xenon + 5% carbon dioxide @ 1.86 atm
Energy range	1.5–37 keV
Energy resolution	18% FWHM at 5.9 keV
Time resolution	980 μs

TABLE 3.2
Specification for the ROSAT PSPC (Pfeffermann *et al.*, 1986)

Sensitive area	8 cm diameter
Drift and absorption region	8 μm
Window	1 μm polypropylene with 50 μg/cm^2 carbon
Fill gas	65% argon+20% xenon+ 15% methane @ 1.5 atm
Energy range	0.1–2.0 keV
Energy resolution	43% FWHM at 0.93 keV
Spatial resolution	250 μm at 0.93 keV
Time resolution	120 μs

individually or in small groups, to separate preamplifiers and noting which channels trigger and the amplitude of their signals, the original interaction site can be recovered with high precision. This is the so-called center of gravity technique (Bateman, 1984) as depicted in Figure 3.5(a) and utilized on the position-sensitive proportional counter (PSPC) at the focus of the grazing incident telescope of the ROSAT satellite (Pfeffermann *et al.*, 1986) Details of this instrument are given in Table 3.2. Other schemes which are employed include coupling the cathodes to delay lines and measuring the delay in arrival time at the ends of each line, as shown in Figure 3.5(b), or connecting successive cathode wire groups through resistors and measuring how this distributed resistance, coupled with the capacitance of each wire subgroup, modifies the rise time of the signal as a function of position in the detector (Figure 3.5(c)).

An alternative technique derives both coordinates from the lower cathode plane which is solid rather than a plane of wires. On this is imprinted an interleaved array of conducting electrodes with a pattern similar to that found on a backgammon board. The electrodes are arranged so that the area of each varies with x and y position on the cathode plane; hence the magnitude of the pickup on any one electrode set relative to the total signal is location dependent (Seigmund, 1983). This so-called wedge and strip technique is capable of providing high spatial resolution for both coordinates, with a single readout plane and only three or four amplifiers. It works particularly well for small-area devices where the large inherent capacitance of this type of readout is not a problem. A wedge and strip readout system is currently being developed for an imaging proportional counter at the heart of the SXRP polarimeter scheduled to fly aboard the Russian Spectrum-X-Gamma Spacecraft (Watkins *et al.*, 1990).

The ultimate spatial resolution limit is set by diffusion in the detection gas and the finite range of the initial photoelectron and de-excitation products (fluorescent photons, Auger electrons). The former is the dominant factor at low energies where

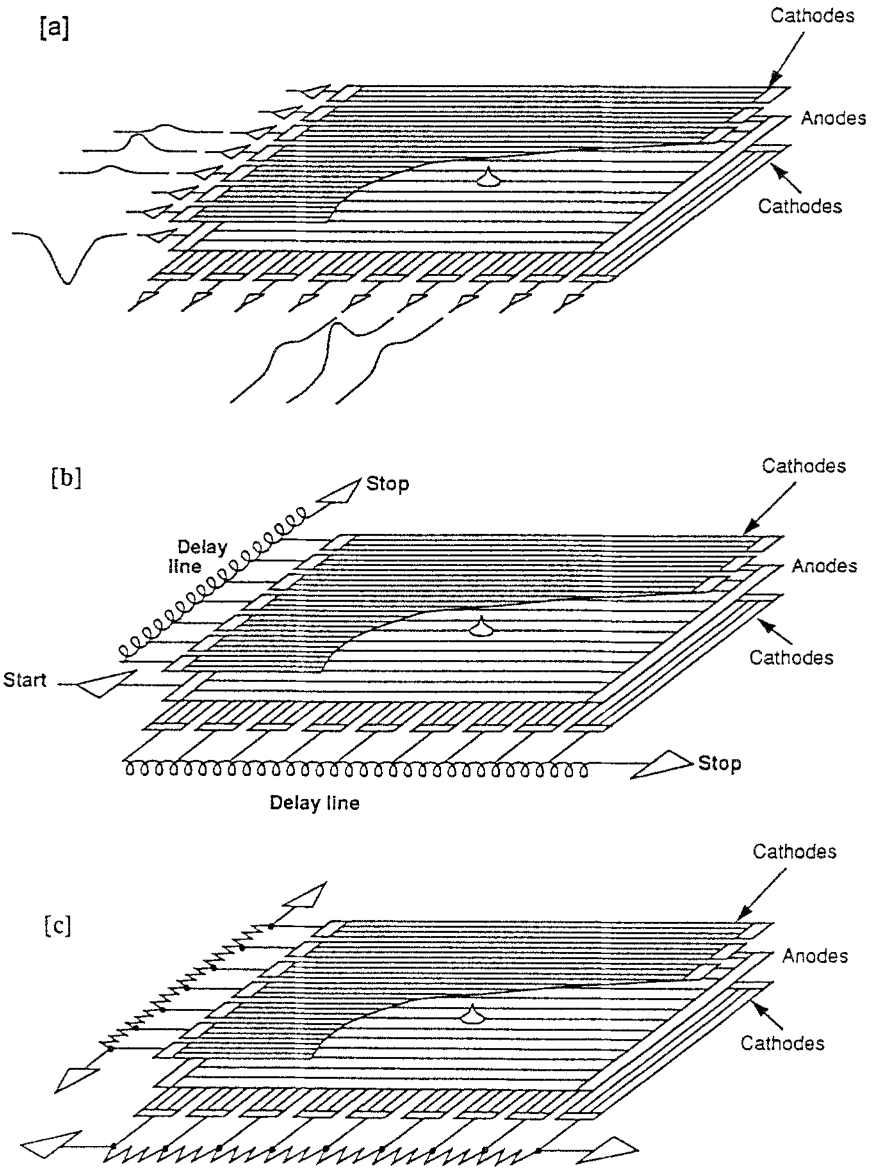

Fig. 3.5. Various schemes used for the position readout of cathode signals in the Multiwire Proportional Counter (MWPC) (see text).

the lateral spread of the charge cloud due to thermal motion of the electrons and the small number of electrons within the cloud makes the determination of the exact centroid imprecise. Typical diffusion limits, which scale as the square root of the drift distance divided by pressure, are around $\frac{1}{10}$ mm FWHM at 6 keV for a few cm drift in 1 atm of gas. At higher energies, the ejected photoelectron has a

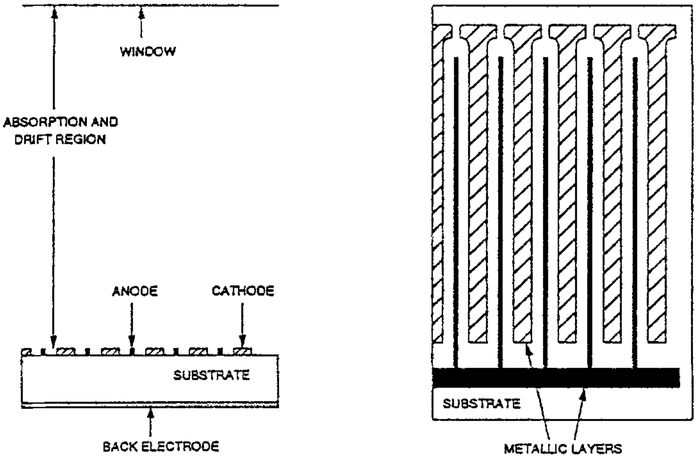

Fig. 3.6. Schematic of a microstrip proportional counter.

non-negligible range and this quickly dominates the spatial resolution. At 30 keV the spatial resolution is several mm in 2 atm of argon and at 60 keV it is more than 1 cm. (Ramsey and Weisskopf, 1987). If high spatial resolution is required at high energies, then heavier gases must be used at elevated pressures to reduce the electron track length. In 10 atm of xenon, the spatial resolution at 100 keV would be sub-millimeter.

While the modern MWPC is highly developed and bears little resemblance to the original single wire proportional counter, further improvements are still being sought. The desire to improve the timing properties of the MWPC for particle research led to the development of the microstrip proportional counter which has many features desirable for astronomy. In these devices, the usual discrete anode and cathode wires are replaced by conducting strips on a partially insulating substrate (Figure 3.6). Fabricated using integrated circuit-type photolithographic processes, they offer very high spatial accuracies and uniformity together with the capability of producing extremely fine electrode structures down to the 1 micron level. This is far beyond the 12.5 micron mechanical limit for wires in practical counters. As the energy resolution of MWPCs is often dominated by geometrical inaccuracies in wire placement, which affect the electric field from wire to wire, as well as anode uniformity and diameter, microstrip proportional counters offer the promise of superior energy performance; $<$ 11% FWHM at 6 keV has already been reported, along with reduced operating voltages, faster signal rise times (due to the very intense fields around the ultra-fine anodes), and the reduced likelihood of wire breakage (Ramsey, 1992). Microstrip-based imaging proportional counters are currently being developed for the focal plane instruments of the SODART telescopes on board the Spectrum-X-Gamma mission (Budtz-Jorgensen *et al.*, 1992), and others are being developed for hard X-ray astronomy from high-altitude balloons (Fulton *et al.*, 1993).

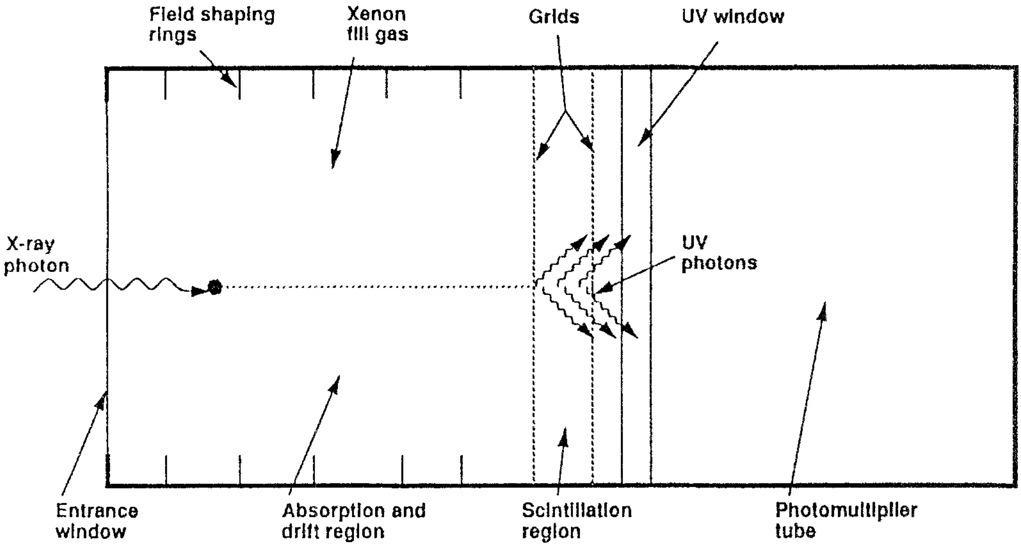

Fig. 3.7. A conventional Gas Scintillation Proportional Counter (GSPC) with absorption and drift volume.

3.2.4. Gas Scintillation Proportional Counters

The gas scintillation proportional counter (GSPC) is a variant of the standard proportional counter in which the electric field is kept just below that necessary for charge multiplication (Policarpo *et al.*, 1972). Under these conditions the primary electrons drift into a high field region and each gains enough energy to excite the fill gas atoms but not to ionize them. This results in a flash of characteristic ultraviolet photons whose intensity is proportional to the energy of the initial X-ray. This scintillation light, which is around 150–200 nm for pure xenon, typically contains tens of thousands of photons and is registered by quartz window photomultiplier tubes (Fraser, 1989). Figure 3.7 gives a schematic representation of a typical GSPC.

The attraction of the GSPC derives from the fact that the emission of scintillation photons is a series of completely independent events and therefore the energy resolution is dependent on the statistics of the final number of photons collected. This is in contrast to the standard proportional counter where the statistics are set not by the final number of electrons but by fluctuations at the beginning of the avalanche process. In the limit, for large light yield and good collection efficiency, the resolution of the GSPC can approach the Fano limit described in Section 3.1 and thus can be a factor of 2 better than the standard proportional counter.

The geometry of the GSPC, as shown in Figure 3.7, is very similar to that of the MWPC with a low field absorption and drift region and a high field scintillation region which is normally defined by a parallel pair of grids and spans several mm to enhance the light yield. Sometimes these two regions are combined into a so-called 'driftless' GSPC having a high field throughout the whole detector volume

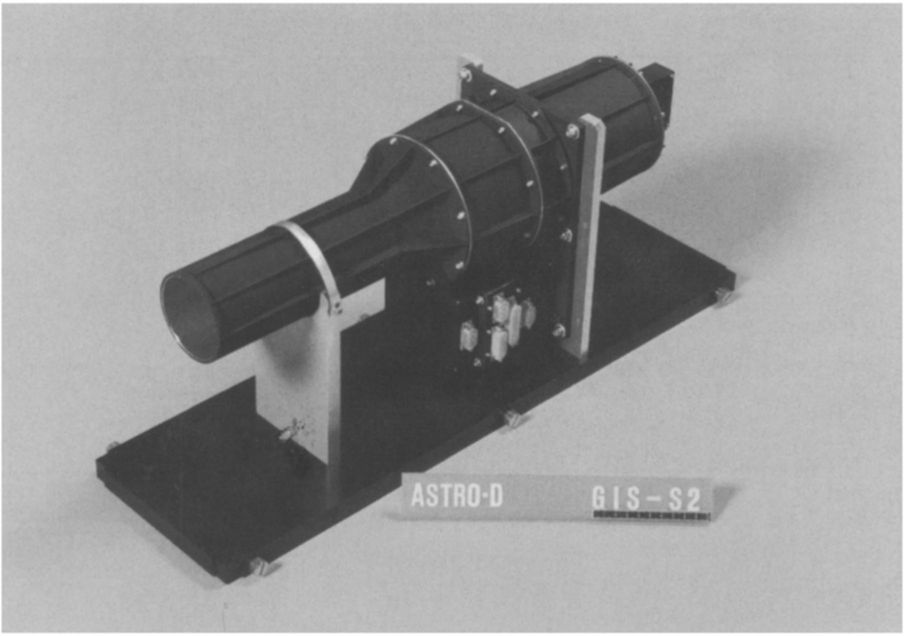

Fig. 3.8. A gas scintillation proportional counter on board the ASCA (Astro-D) spacecraft (Courtesy of K.Makishima, University of Tokyo).

(Simons *et al.*, 1985). In this configuration the amount of light produced for a given input energy is variable and depends on the penetration depth of the initial X-ray. The original energy is then recovered by measuring not only the light yield but the duration of the light signal or burst length. The advantage of the driftless GSPC is that the interior electric field is very high throughout and this ensures rapid registration of each event before any losses of charge can take place to the entrance window or to electronegative contaminants in the detector gas. It also removes the need for drifting through grids delineating the drift and scintillation region which can also result in charge loss.

The original GSPC was developed in 1972 and since then several instruments have been flown on sounding rockets and satellites. The GSPC on board the EXOSAT satellite was a non-imaging device with an effective area of 100 cm^2 which operated over the energy range 2–40 keV. Its energy resolution was 10% at 6 keV (Peacock *et al.*, 1981) Imaging GSPCs are actively being developed and there are a number of schemes for position sensing. A common arrangement is to use some form of imaging photomultiplier tube to determine the centroid of the light distribution. Such a technique is used on the driftless imaging GSPC being developed for the focal plane of an X-ray telescope on the Italian SAX mission (Favata *et al.*, 1989) and for the conventional GSPC used as a focal plane instrument on the Japanese ASCA mission (Ohashi *et al.*, 1991). Details of these two instruments are given in Table 3.3 and an ASCA flight unit is shown in Figure 3.8.

A large-area high-pressure imaging GSPC is also being developed for use on

TABLE 3.3
Characteristics of the GSPCs for the ASCA (Ohashi *et al.*, 1991) and SAX (Favata *et al.*, 1989) missions

	ASCA	SAX (LEGSPC)
Effective area	50 mm diameter	30 mm diameter
Effective range	0.7–20 keV	0.1–10 keV
Energy resolution (5.9 keV)	$< 8\%$ FWHM	7.0%
Position resolution (5.9 keV)	0.5 mm	0.9 mm
Time resolution	61 μsec	–

a high-altitude balloon platform. This device will have a sensitive area of over 1000 cm^2 and will contain a 22 cm depth of xenon gas at 20 atm pressure (Sadoulet *et al.*, 1989). To avoid the mechanical problems of large-area ultraviolet transmitting windows it utilizes a novel position-sensing read-out scheme consisting of crossed arrays of wave shifting fibers which exit the pressure vessel and are read out by an array of phototubes. The instrument is designed to operate from the atmospheric cut-off point, 20–30 keV, up to several hundred keV.

3.3. MICROCHANNEL PLATES

A variant of the standard photomultiplier tube is the channel electron multiplier (Knoll, 1989). This device can be viewed as a photomultiplier tube with a continuous dynode running its entire length (when operated in a vacuum). Electrons liberated at the front end of the channel multiplier, through the interaction of incident X-ray photons, are accelerated down the tube by the applied potential, repeatedly striking the specially-coated tube walls. Each hit generates several secondary electrons which also are accelerated down the tube and, in turn, produce further electrons of their own as shown in Figure 3.9(a). In this manner a cascade of electrons is produced which eventually emerges from the end of the multiplier tube.

Large numbers of these channels can be bundled together to form a microchannel plate (MCP), with each channel still acting as an independent multiplier (Figure 3.9(b)). Typical plates have individual channels of diameter 12.5–25 μm, and have thicknesses of a few mm and areas of 10–100 cm^2 (see Figure 3.10). They are formed by taking a hollow rod of lead glass (glass containing up to 50% by weight of lead oxide) and inserting a core of etchable material, usually another type of glass. The assembly is then drawn to produce a fiber of order 1 mm diameter, and these are then cut and stacked to form a bundle of hexagonal cross section. Individual bundles are then further drawn, stacked and heated in an oven to fuse the assembly, which is cut and polished to the desired configuration. The final step is to etch away the channel interiors and deposit contact electrodes and a suitable channel coating to ensure a high secondary electron yield for charge multiplication

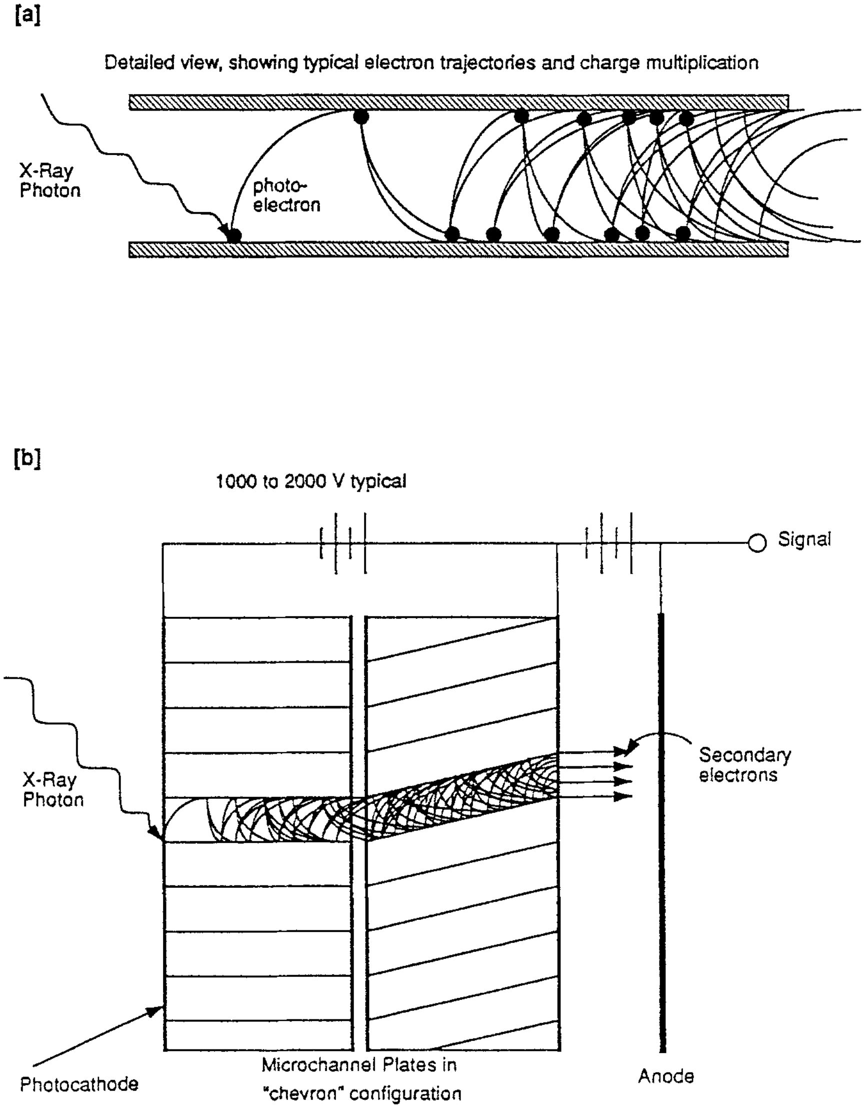

Fig. 3.9. Schematic of the operation of a Microchannel Plate (MCP). In (a) the charge multiplication process in a single channel is shown and in (b), a typical configuration for a pair of plates is shown (From Knoll, 1989.)

(Fraser, 1989).

In operation, very large gains are possible with the MCP provided steps are taken to minimize positive ion feedback. This is caused by residual gas atoms in the channels being ionized by the avalanche and then traveling back up the channel where they can initiate large after-pulses through collisions with the walls. The simplest way to avoid this is to not let the ions 'see' back to the start of the channel, where they would have a maximum effect, and this is usually accomplished by

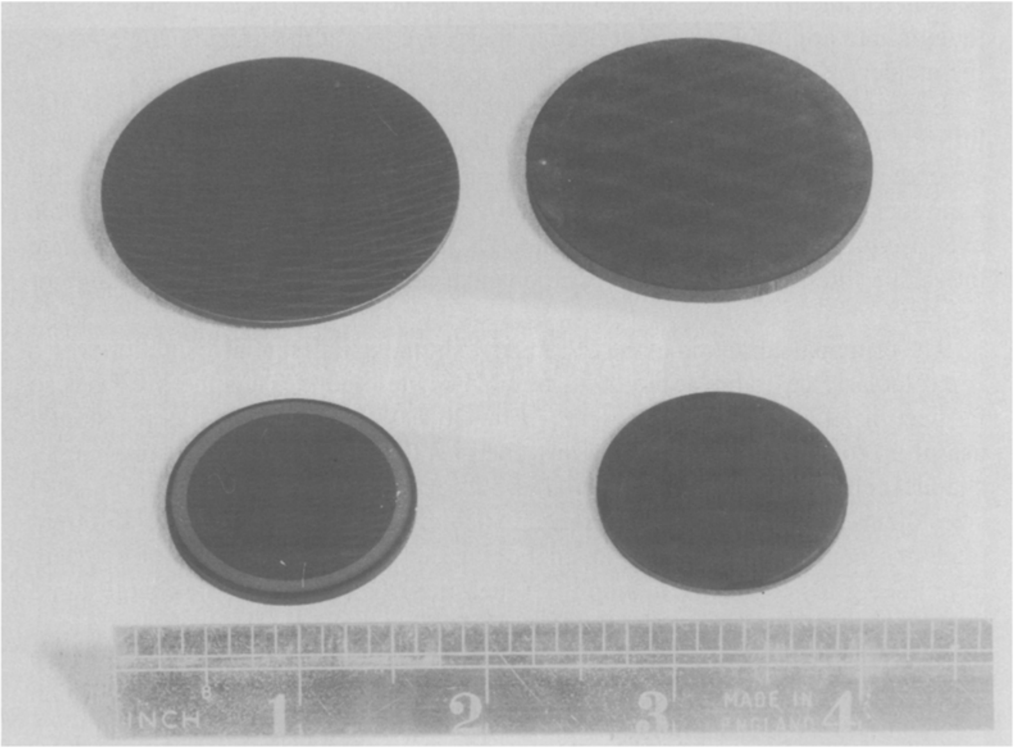

Fig. 3.10. Some typical microchannel plates (Courtesy of George Fraser, University of Leicester).

utilizing two plates in a chevron configuration with a small ($\sim$1 mm) gap in between (see Figure 3.9(b)). The plates are usually biased at an angle of order 15° with respect to each other. A second, though not so widely-used technique is to employ curved microchannel plates. With positive ion feed-back controlled in this manner, gains of greater than 10^7 are possible before saturation sets in. This saturation occurs when the avalanche depletes the charge from the channel walls and it cannot be replaced on the time scale of the event. This effect also sets the maximum count rate that the device can handle (Fraser, 1989)

Microchannel plates have been used at the focus of X-ray telescopes to provide high resolution imaging. For enhanced response in the soft X-ray region, the front surface of the plate is usually coated with a material having a high electron yield, such as magnesium fluoride. This was the case for both the high resolution imager (HRI) on the *Einstein* satellite (Henry *et al.*, 1977) and for the channel multiplier array on EXOSAT (de Korte *et al.*, 1981a) More recently, cesium iodide has been found to offer further enhancements in quantum efficiency, and this material was used for the microchannel plate at the heart of both the ROSAT HRI and wide field camera (WFC) (Pfeffermann *et al.*, 1986). Quantum efficiencies as high as 30–40% are possible for cesium iodide coated plates compared with only a few percent for uncoated ones. This efficiency is dependent upon incident photon angle though, and approaches zero at normal incidence and at the grazing angle where the incident X-ray is reflected rather than absorbed in the channel coating.

Even when operated below the saturation limit the microchannel plate has little or no energy resolution. With cesium iodide coating the output signal is dependent upon the energy of the incident photon, but the spread in signal sizes for a monoenergetic input is so large that only two or three energy bins are possible over a typical 10–20 keV energy band. The usual course of action is to include moveable filters in front of the microchannel plate to select the energy range of interest.

The principal attraction of the MCP is its extremely high spatial resolution which is particularly desirable at the focus of an X-ray telescope. Thus the MCP has so far been used at low X-ray energies (<10–20 keV) even though it is potentially useful up to hundreds of keV. At low energies the X-rays penetrate only single-channel cells, and the resulting spatial resolution can be on the order of the channel sizes themselves, i.e., tens of microns. To achieve this resolution several different readout schemes have been employed. For the Einstein and ROSAT HRIs, a system of crossed grids connected to amplifiers measured the centroid of the charge cloud exciting the MCP, whereas, for the ROSAT WFC, a resistive disc was used. Here, the charge signal was registered by four amplifiers located around the periphery of a resistive collection electrode. By taking suitable ratios of the signals, which are modified by the distributed resistance between the collection site and each amplifier, the position can be determined with high precision. The resulting spatial resolutions were 33 and 20 μm FWHM, respectively, for the Einstein and ROSAT HRIs and 100 μm FWHM for the ROSAT WFC (see Fraser, 1989, and references therein for a more detailed account of position sensing techniques).

The largest MCP under construction for X-ray astronomy is that for the high resolution imaging camera (HRC-I) intended for the AXAF-I mission (Murray *et al.*, 1987) which is currently scheduled for launch in 1998. This device has linear dimensions of 10 × 10 cm, a pore size of 12.5 μm, and utilizes a crossed grid readout with 65 amplifiers per axis to determine the charge centroid to an accuracy of better than 25 μm. Details of the HRC are given in Table 3.4.

Finally, in order that they can provide the highest sensitivities for X-ray astronomy, the MCPs must have extremely low backgrounds. Early work showed that most MCPs had a common background level regardless of the specific details of the instrument and this was later found to be due to radioactivity, in particular K^{40}, in the glass used for the construction (Fraser *et al.*, 1987). A development program is currently underway to produce low background plates for use in future missions such as AXAF.

TABLE 3.4
Details of the proposed AXAF Imaging High Resolution Camera (HRC-I)

Configuration	Chevron pair, 6° bias front, −6° bias rear, 50 μm gap between plates
Area	10×10 cm
Geometry	12.5 μm pixels, 15 μm pitch
Photocathode	Cesium iodide
Readout	Crossed grids, 65×65 pre-amplifiers
Spatial resolution	Better than 25 μm FWHM
Time resolution	16 μs
Background rate (low noise glass)	6×10^{-3} counts cm^{-2} s^{-1} (internal)
Bandwidth	0.1 to 10 keV

3.4. SEMICONDUCTOR DETECTORS

3.4.1. Introduction

The advantage of semiconductors over other solid materials for detecting radiation is the ease with which information carriers, in this case electrons and holes, can be formed by the absorption of radiation. Semiconductors are crystalline materials distinguished from metals by an energy band structure consisting of three regions: the valence band, the forbidden gap, and the conduction band (Figure 3.11). The valence band is the lowest energy band and is filled with bound electrons which are unable to drift through the crystal. The forbidden gap spans the range of electron energies forbidden by quantum mechanics. The conduction band corresponds to the energies of electrons which are free to move throughout the crystal lattice. The difference in energy between the lowest energy electron in the conduction band and the highest energy electron in the valence band is called the bandgap E_g. The bandgap is the most important parameter in semiconductor physics. For a semiconductor, E_g is typically about 1 eV. Equation (8) gives the number density of thermally-generated electron-hole pairs as a function of the bandgap energy.

$$n = CT^{3/2}\exp(-E_g/2kT)\,, \tag{8}$$

where C is a proportionality constant that depends on the material, T is the temperature in Kelvin, E_g is the bandgap energy, and k is the Boltzmann constant. In semiconductors at room temperature some electrons in the valence band can be thermally excited into the conduction band and the conduction band is partially filled. Insulators have bandgaps larger than 5 eV and have an empty conduction band.

A material in which electrons are majority charge carriers is designated n-type; if holes are the majority carriers, the material is p-type. A hole is a vacancy formed when an electron in the valence band is excited into the conduction band. An electron-hole pair is the solid state analog of an ion pair produced in a gas-filled

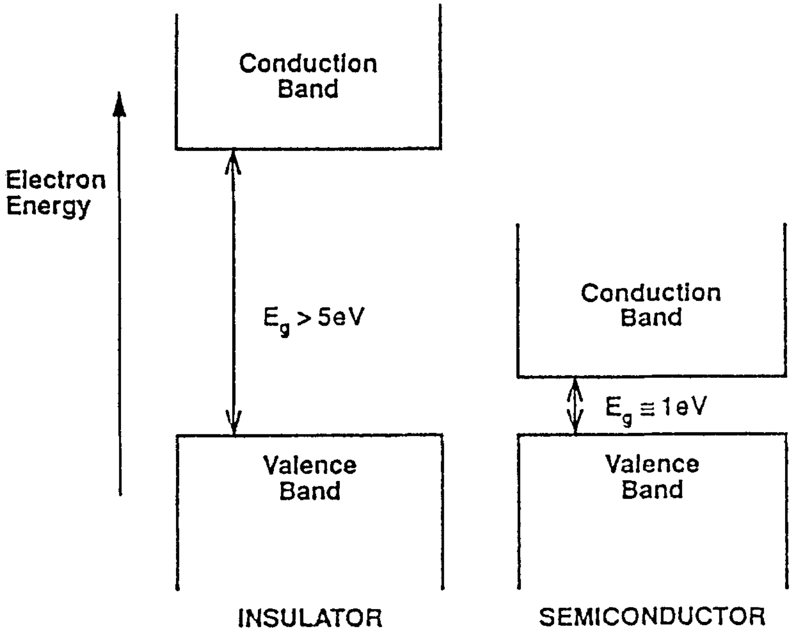

Fig. 3.11. Illustration of the band structure for insulators and semiconductors.

ionization chamber. When a photon is photoelectrically absorbed in a semiconductor, the ejected photoelectron loses approximately two-thirds of its energy as heat and the remainder goes into the formation of electron-hole pairs. The short photoelectron path lengths in solids makes possible quite good spatial resolutions: ~250 μm for a 30-keV X-ray in Si. The energy required to form an electron-hole pair (2–5 eV) is approximately 3 times the bandgap energy; this compares favorably with energies in excess of 20 eV required to form ion pairs in gases. The Fano factors for gases and semiconductors are of comparable magnitude (~0.1). Thus the small amount of energy required to produce electron-hole pairs in solid state detectors translates into potentially better energy resolution than most other detector technologies. For a typical semiconductor, one would ideally expect an energy resolution of approximately 200 eV (FWHM) at 20 keV. Since semiconductor detectors are not amplifying devices like proportional counters, energy resolution is degraded by the noise from the amplifying electronics. Further noise comes from system capacitance and fluctuations in the leakage current flowing through the detector (shot noise). Also, imperfect charge collection (discussed below) will further degrade the energy resolution.

At the present time, Si and Ge are the materials most often used in semiconductor detectors for X-ray astronomy. Unfortunately, as a result of their narrow band gaps, these materials must be kept at low temperatures to reduce thermally generated noise. Since refrigeration equipment tends to be heavy and bulky, and

TABLE 3.5
Important physical properties of some semiconducting materials used in X-ray detectors

Semi-conductor	Atomic Nos.	$\mu_e\tau$ (cm^2 v^{-1})	Bandgap (eV)	Fano factor (typical values)	Energy per electron-hole Pair (eV)
Si	14	$>10^{-1}$	1.12	0.1 (Rossington *et al.*, 1992)	3.61
Ge	32	$>10^{-1}$	0.74	0.08 (Rossington *et al.*, 1992)	2.98
HgI_2	80, 53	$<10^{-4}$	2.13	0.20 (Dabrowski *et al.*, 1983)	4.22
CdTe	48, 52	$<10^{-3}$	1.47	–	4.42

hence expensive to put on a spacecraft, semiconductors with bandgaps sufficiently large to operate at room temperature are much sought after. For hard X-ray spectroscopy, it is important to find semiconducting material with high values of Z (atomic number). A high value of Z is desirable as it ensures a high photoelectric cross section so that all the incident energy is more likely to be absorbed in the detector. For example, in the case of Si, the Compton cross section exceeds the photoelectric cross section for energies above 50 keV; a high background from Compton scatters makes it difficult to make a precise energy measurement. HgI_2 and CdTe are two materials which have attracted a great deal of interest since the 1970's. Work on these two materials has continued up to the present time, but progress has been slow due to their limited applications outside X-ray detector technology. The major hurdle has been to produce high quality crystals having good charge transport properties (measured as the mobility-lifetime product for electrons, $\mu_e\tau$). The mobility-lifetime product is a measure of how efficiently charges in a semiconductor can be collected at an electrical contact. Unless the detector is kept very thin, a small value of $\mu_e\tau$_means that charges will be lost en route to their collection point, and energy resolution, which depends on the number of charges collected, will be poor. As seen in Table 3.5, CdTe and HgI_2 have small values of $\mu_e\tau$ compared to both Si and Ge; fortunately, the former have sufficiently large bandgaps which allow room temperature operation. For some applications, the convenience of not refrigerating the detector combined with high absorption efficiency more than compensates for inferior energy resolution.

3.4.2. Slab with Ohmic Contacts

The simplest radiation detector made from a semiconducting material would consist of a slab of semiconductor with metallic contacts deposited on opposite faces of the material (Figure 3.12(a)). The metal contacts simply provide electrical connection to the semiconductor and are called ohmic contacts. If a potential is applied to such

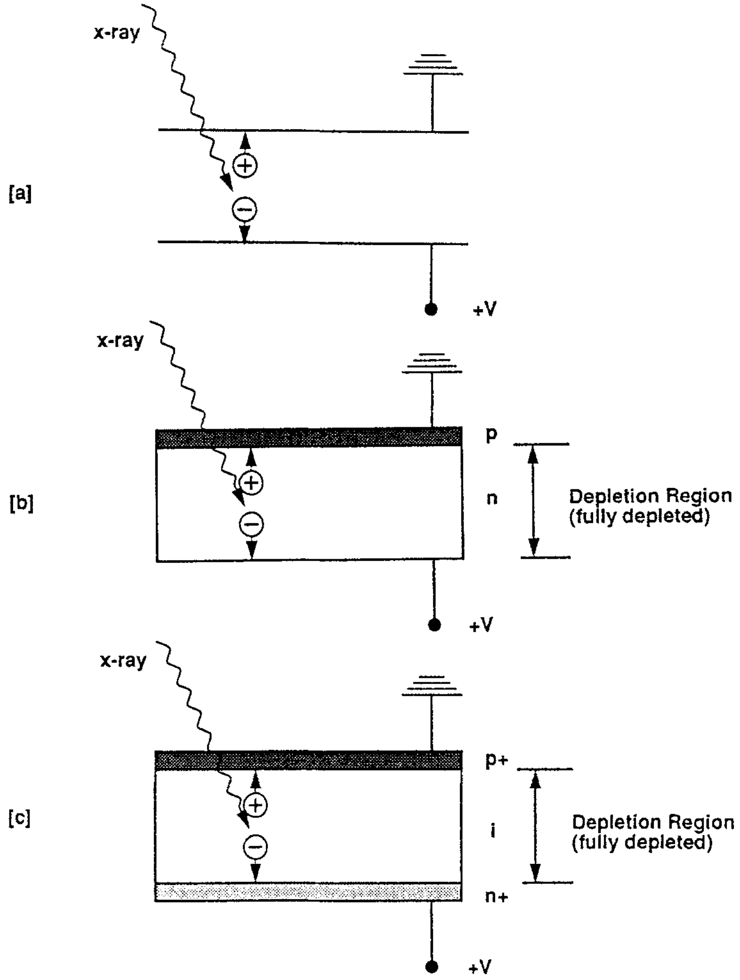

Fig. 3.12. Different types of semiconductor detectors; (a) A slab with ohmic contacts, (b) A PN junction, and (c) A PIN diode detector.

a device, electrons and holes liberated by absorbed radiation would drift to opposite contacts and the collected charge would be proportional to the energy absorbed. Such a device would be a direct semiconductor analog to a gaseous ionization chamber.

Because of its large bandgap (2.2 eV), HgI_2 benefits from very low leakage current at room temperatures, so detectors made from this material take the form described above. Up to now, HgI_2 is the only semiconductor other than Si and Ge known to be used for X-ray astronomy. The balloon experiment of Ogawara *et al.* (1982) flown in 1980, used a detector containing eleven HgI_2 crystals to detect radiation from the black hole candidate Cyg X-1 (see Table 3.6). The advantages of a high-Z absorber were demonstrated in a second flight in 1982, where the background rate in HgI_2 was found to be a factor of 5 times lower than with NaI/CsI or Ge systems sized for an equivalent efficiency in the energy range of 40 –80 keV (Vallerga *et al.*, 1982).

TABLE 3.6
Characteristics of the HgI_2 detector flown aboard the balloon experiment of Ogawara *et al.* (1982)

Area	7.6 cm^2
Crystal thickness	750 μm
Absorption efficiency	~ 50% @ 100 keV
Energy range	20 to 100 keV
Energy resolution	between 2 and 6 keV @ 60 keV

3.4.3. *PN Junctions*

Unfortunately, for common semiconductors like silicon and germanium with a relatively low resistivity, a detector simply consisting of a slab with ohmic contacts would suffer from excessive shot noise. Shot noise is the noise resulting from fluctuations in charge collected from the leakage current during the measuring time of the signal processing electronics.

To significantly reduce the leakage current, a diode can be made from an intrinsically n-type or p-type material by having one face doped with an impurity to form a p-type or n-type layer, respectively (Figure 3.12(b)). When reverse biased, the PN junction provides high resistance to current flow and hence very little leakage current. Equilibrium between carrier diffusion and internal electric fields will produce a high resistivity region called the depletion region. The depletion region corresponds to the sensitive depth of a semiconducting detector. The size of the depletion region, d, is proportional to the square root of the product of the resistivity, ρ, of the semiconductor and the voltage applied across the junction, V,

$$d \cong (2\varepsilon V \mu\rho)^{0.5} , \tag{9}$$

where ε is the dielectric constant and μ is the mobility of the majority carriers. By increasing the voltage, the depletion region can be increased until it extends fully through the semiconductor, i.e., the detector is fully depleted or until the breakdown voltage for the semiconductor has been reached.

3.4.4. *Pin Detectors*

For silicon with the highest currently available purity, the maximum depletion depth attainable is 1–2 mm before breakdown occurs. One can see from equation (9) that the voltage required to achieve a desired depletion depth is inversely proportional to the resistivity of the semiconductor. To increase the maximum obtainable depletion depth of a semiconductor detector, an alkali metal such as lithium is diffused through high-purity silicon or germanium to neutralize excess charge carriers and create a region of intrinsically high resistivity; i.e., the semiconductor has been compensated. Lithium drifted silicon and germanium are referred to as Si(Li) and Ge(Li), respectively. A so-called intrinsic semiconductor is one in which all (or

TABLE 3.7
Physical characteristics of the detector used on BBXRT

Detector type	Segmented Si(Li)
Area	28 cm^2
Energy range	0.5 to 12.0 keV
Energy resolution	$\sim$ 185 eV @ 5.89 keV

practically all) charge carriers in the conduction band are produced by thermal excitation (see Equation (8)). The diffusion process naturally forms what is called a PIN (p-type-intrinsic-n-type) detector (Figure 3.12(c)). The face of the material in contact with the lithium becomes heavily doped n-type (represented by n^+) and can act as an electrical contact. The bulk of the semiconductor has a uniform concentration of lithium atoms which mop up excess holes resulting in very few charge carriers; this region acts as though it were intrinsic. The uncompensated face of the detector is p-type and is often coated with metal to form an ohmic contact. The PIN detector is reverse biased as is the PN diode with the intrinsic region determining the sensitive volume of the detector.

The Broad Band X-Ray Telescope (BBXRT) which flew aboard the Space Shuttle *Columbia* in 1990 used nested, conical mirrors to focus X-rays on a segmented Si(Li) detector having five elements (Figure 3.13). Segmentation was achieved by cutting grooves into the face of a monolithic Si(Li) diode. By subdividing a large, 3 cm diameter diode, better energy resolution was achieved through the reduction of capacitance. Segmentation also provided spatial information unavailable from single pixel detectors. The detector characteristics are summarized in Table 3.7. When observing weak, point sources, background was suppressed by rejecting events having inner and outer pixel coincidences (Serlemitsos *et al.*, 1984).

The Silicon X-ray Array (SIXA) is planned to be flown on the Spectrum-X-Gamma mission (Sipila *et al.*, 1991). SIXA will be composed of 19 discrete circular Si(Li) detectors, closely packed, to provide imaging sensitivity, over the energy range 0.5–20 keV, in conjunction with a grazing incidence mirror. The estimated resolution of the instrument is 170–180 eV at 6 keV. SIXA will be passively cooled to 105–110 K and a thin window of aluminum-coated polyimide between SIXA and the telescope mirror will reduce thermal losses as well as shield the detector from UV and visible light.

Because of the high mobility of lithium in silicon and germanium detectors, the lithium ions gradually redistribute themselves due to internal electric fields. In germanium the mobility of lithium is sufficiently high to require that Ge(Li) detectors be kept at liquid nitrogen temperature (77 K) at all times to avoid decompensation. Si(Li) detectors can be kept at room temperature for short times without deleterious effects. Apart from the need to avoid lithium redistribution,

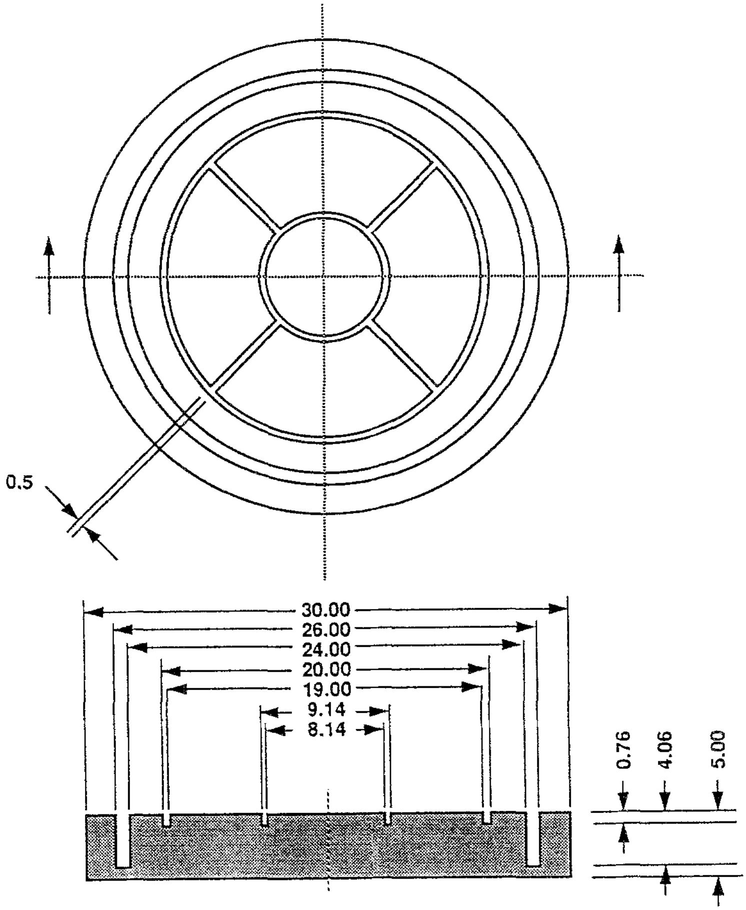

Fig. 3.13. Segmented Si(Li) detector for the Broad Band X-Ray Telescope (BBXRT).

Si(Li) and Ge(Li) detectors are kept at liquid nitrogen temperatures during operation to improve energy resolution by reducing leakage current. Because of its extreme instability at room temperature, Ge(Li) has been supplanted in recent years by high purity germanium (HPGe) which is sufficiently pure to form detectors having equivalent sensitive volumes to its unstable predecessor.

The solid state spectrometer flown aboard the Einstein Observatory consisted of parallel HPGe and Si(Li) diodes operated in anticoincidence to reduce the background due to charged particles. The detector was designed to cover an energy range from 0.5 to 5 keV (Joyce *et al.*, 1978). A passive refrigeration system maintained an operating temperature of around 100 K and the detector achieved an in-flight energy resolution of 160 eV (FWHM) at 5.9 keV.

The Gamma Ray Imaging Spectrometer (GRIS) observed SN 1987A during April and October 1988 (Tueller, 1990). The balloon-borne detector consisted of an array of seven HPGe cylindrical detectors which will eventually be used with a coded aperture mask for imaging. GRIS was flown again in April and May of 1992 from Alice Springs, Australia. For this flight, the Ge detectors were replaced with isotopically enriched ^{70}Ge cylinders which, having a low cross section for

TABLE 3.8
Physical characteristics of the detectors used on GRIS

Detector type	HPGe (96% ^{70}Ge)
Area	242 cm^2
Energy range	15 keV to 10 MeV
Energy resolution	$\sim$ 2 keV @ 1 MeV

neutron activation, suppressed background by a factor of 2 (Gehrels, 1992a) (For a summary of GRIS properties, refer to Table 3.8.) A spectrometer similar to GRIS but containing nineteen detectors is included in a plan for the European Space Agency's INTErnational Gamma Ray Astrophysics Laboratory (INTEGRAL).

At least one group, in Italy, is studying the properties of two-dimensional arrays of CdTe detectors for astronomy (Casali *et al.*, 1992). To achieve high absorption efficiency while maintaining reasonable energy resolution (2% at 511 keV), rectangular bars of CdTe (2 × 2 × 10 mm) are oriented so that incident radiation is absorbed along their long dimension and are biased so that the applied electric field is along the small dimension of each bar. In the future, this group plans to expand their current array of five diodes to construct a large-area detector to image cosmic sources of the electron-positron annihilation line at 511 keV.

3.4.5. CCDs

A charge coupled device (CCD) is a solid state imaging device which typically consists of a closely-spaced array of MOS (metal-oxide semiconductors) capacitors formed by sandwiching an insulating oxide layer between a heavily doped region of semiconductor (*p*-type silicon) and a metal electrode (Figure 3.14). Positive bias is applied to all electrodes to produce surface depletion. Electrons generated by photoelectric absorption of X-rays in the semiconductor are stored until an increasing voltage on an adjacent electrode forms a deeper potential well and the electrons are transferred to that electrode. By continuing this process, charges are transferred from pixel to pixel until the entire device is read out (Sze, 1985).

The AXAF CCD Imaging Spectrometer (ACIS) will be a core focal plane instrument for AXAF-I. ACIS will consist of two CCD arrays: a two-dimensional imaging array and a linear array for spectroscopy. The imaging array will have four CCDs and will cover 295 square arc min on the sky. To provide almost seamless coverage of the whole image, the CCDs are each read out from only one side; hence, they are abuttable on three sides. The spectroscopic linear array will likely consist of six CCDs (Garmire *et al.*, 1988) which will be used to separate orders in a spectrum produced by a grating. (For a summary of the ACIS CCDs, see Table 3.9.)

High resistivity silicon (10 000 Ohm-cm) allows the CCDs to be depleted to a

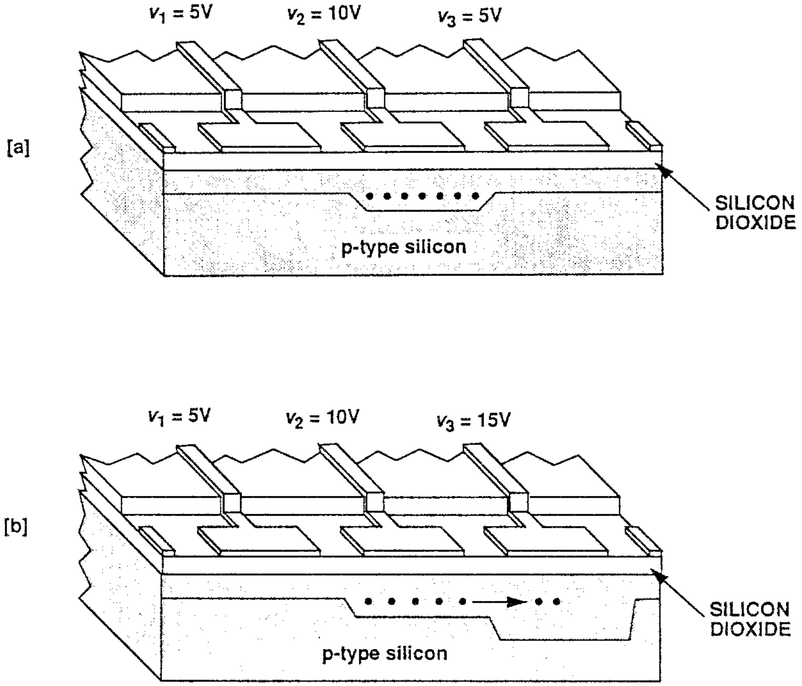

Fig. 3.14. Diagram illustrating how charge is transferred in a three-phase charge coupled device (CCD). (a) Electrons lie in the potential well formed by high voltage on v_2. (b) Increased voltage on v_3 causes charge to be transferred to the lower potential region.

TABLE 3.9
Parameters of ACIS CCDs

Number of pixels	1024 × 1024
Pixel size	$25 \times 25\ \mu\text{m}^2$
Time resolution	54 μsec to 6 msec
Energy range	0.1 to 10 keV
Energy resolution	140 eV @ 5.9 keV

depth of 50 μm which will give a high detection efficiency in AXAF's energy band; at 5.9 keV, for example, ACIS will absorb 80% of the incident X-rays. Many cosmic ray particles produce large signal pulses across several pixels because of their high energies and long path lengths in silicon. By rejecting such multi-pixel events, more than 99% of the cosmic ray background can be eliminated. The combination of gratings and CCD will yield an energy resolution 10 times better than the CCD alone.

Radiation damage from charged particle bombardment in space increases the number of carrier trapping sites in silicon which results in a loss of electrons during readout. Annealing at ~ 100 °C for a number of hours removes much of the

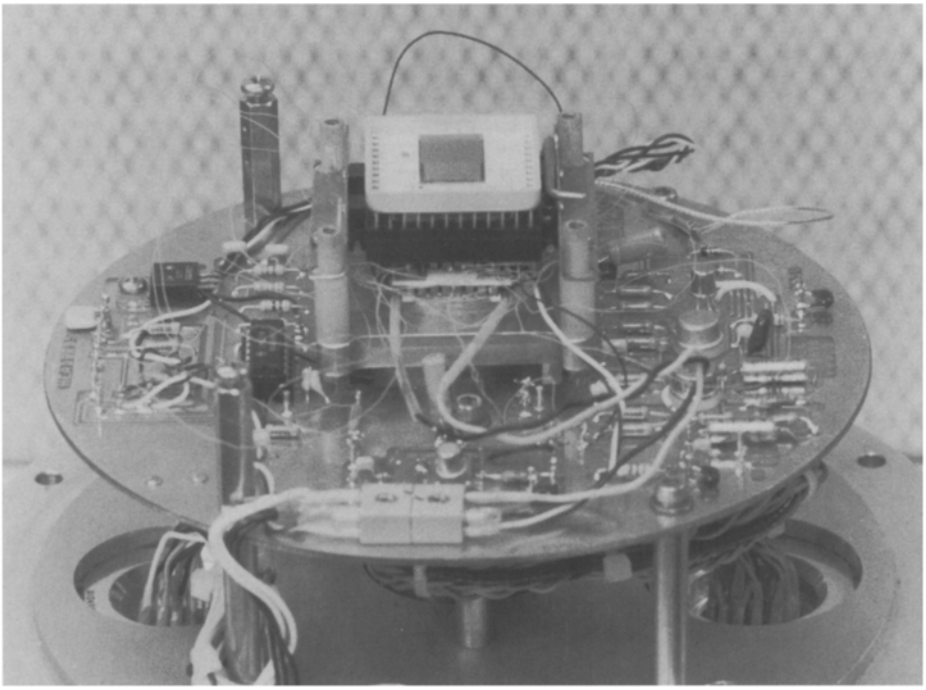

Fig. 3.15. Testing a prototype CCD for the Japanese ASCA mission (courtesy of Gordon Garmire, Penn State University).

radiation damage. Low temperature operation (through passive cooling in space) can improve charge collection efficiency significantly. To minimize the effects of radiation damage, the CCDs are divided into parallel strips, 512 pixels wide and 1024 pixels long with an amplifier attached to both ends of the 512 pixel serial register. Half an image will be read out on the left side of the register and the other half will be read out on the right side. This read-out scheme reduces the distance charge must be transferred and thus makes the CCD less susceptible to radiation damage (Garmire *et al.*, 1991).

Two CCD imaging spectrometers are among the focal plane instruments flown on board the Japanese/US X-ray satellite, ASCA, which was launched on February 20, 1993 (Gendreau *et al.*, 1993). Each spectrometer consists of an array of four 422 × 420 frame-store CCDs with square, 27 by 27 μm, pixels (Figure 3.15). These CCDs are identical to ones originally baselined for the AXAF satellite, and their performance is roughly equivalent to that projected for AXAF in Table 3.9. Up to the time of this article, only a very cursory analysis of some of the images acquired by ASCA has been possible, but it is already obvious that a wealth of spectral detail is being revealed between 1 and 10 keV by this new instrument (Mushotzky, private communication).

A CCD imager will also be flown aboard the European Space Agency's X-ray

Multi-Mirror (XMM) satellite mission planned for launch at the end of the century. Utilizing replicated mirrors (see Section 2.1.2.2) the XMM telescope has a design goal of 30 arc sec angular resolution. A CCD with the resolution of ACIS would over-sample the image by a factor of several thousand. To avoid this, an independent CCD development program was started in which a PN-CCD concept, first proposed in 1984 (Gatti and Rehak, 1984)), was chosen. In this type of CCD, PN junctions replace MOS capacitors and as PN junctions do not suffer as much from surface damage the resulting CCDs are more radiation resistant than conventional devices. The XMM CCD will be a 6×6 cm monolithic device, designed to have a depletion depth of 280 μm, and will achieve an absorption efficiency of 90% at 10 keV, the upper limit of the XMM energy range. A pixel size of 150×150 μm has been chosen as optimal; this corresponds to 8×8 pixels in the mirror's HEW. A smaller pixel size will be chosen if mirror resolution is improved.

3.5. CALORIMETERS

Calorimeters measure energy through the accompanying temperature rise in a suitable absorber. This technique has long been used in nuclear physics to record the energy from radioactive decays and has more recently found widespread use in infrared astronomy where liquid helium cooled bolometers are used to record the thermal emission from cosmic sources. The radical departure for X-ray astronomy is that the device must measure individual photons rather than a continuous flux and thus the temperature rise associated with the absorption of a single X-ray photon must be registered with accuracy.

It can be quickly shown that this technique has the potential for remarkably good energy resolution limited, in an *ideal* case, only by thermodynamic energy fluctuations within the absorber which represent a background against which the temperature rise from the absorbed event must be measured (McCammon *et al.*, 1984). Simple statistical calculations give this limiting resolution as

$$\Delta E = 2.36(kT^2C)^{0.5} , \tag{10}$$

where k is Boltzmann's constant, T is the detector temperature, and C is the detector thermal capacity. A small piece of silicon, 0.5 mm square and 25 μm thick, has a heat capacity of 4×10^{-15} J K^{-1} at 0.1 K, giving $\Delta E < 1$ eV (FWHM). This should be compared with a theoretical limit of approximately 200 eV for a conventional solid state detector (Section 3.4). At 6 keV the absorption efficiency of the above absorber would be greater than 50% and thus a calorimeter, operating at a fraction of a degree Kelvin, offers the potential of an instrument combining high quantum efficiency with the ultra-high energy resolution of a dispersive spectrometer, such as a Bragg crystal or diffraction grating (Section 2.2).

The principal components of a calorimeter are an absorber to convert the incident photon energy to heat, a thermometer to measure the resulting temperature rise and a thermal link to cool the absorber after the event has been registered. A schematic of a typical calorimeter is shown in Figure 3.16.

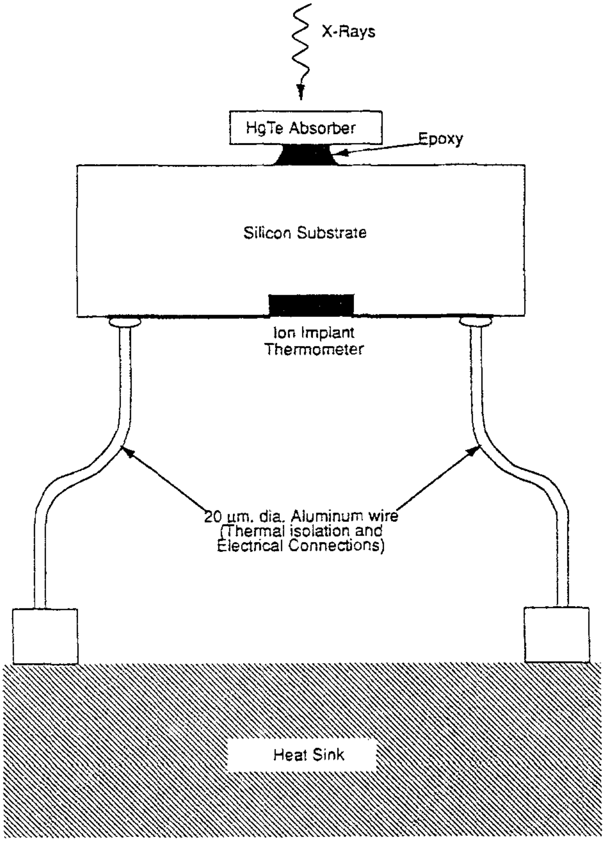

Fig. 3.16. Schematic of the construction of a typical calorimeter.

The absorber must ideally convert all of the incident photon energy to heat. The temperature rise of the absorber is then given by the absorbed energy divided by the thermal capacity of the device. For maximum sensitivity the thermal capacity must be kept at a minimum and this, in turn, necessitates the use of special materials and very small absorbers (typically a fraction of a square mm). The choice of material involves various trade-offs. Silicon has a low thermal capacity and has been used in early devices, but its drawback is that roughly one-third of the absorbed energy does not end up as heat on a useful time scale but goes into forming electron-hole pairs which, in the absence of any drift bias to sweep them free, become trapped at impurity sites and imperfections in the crystal lattice. The energy resolution then becomes dominated by statistical fluctuations in the fraction of energy converted to heat within the integration time of the detector. The ultimate energy resolution with a silicon absorber used in this manner is, then, not that given by the above ideal case formula but in fact only twice as good as that of the silicon semiconductor detector. Investigating other materials, we note that insulators, in general, can be treated as wide band semiconductors with the same attendant problems in conversions of energy to heat. Metals, on the other hand, are very good thermalizers, but have the drawback that they have extremely large heat capacity at low temperatures and so could only be used for very small detectors. To date, the most promising classes of material are zero bandgap semiconductors and semi-metals, and also superconductors. Among the former, mercuric telluride HgTe looks particularly interesting. This material exhibits little or no energy trapping and has returned the best measured results to date as an absorber for single photon calorimeters.

The basic requirement of the thermometer is that it must accurately measure the temperature rise of the absorber with minimal disturbance of the system. Doped semiconductors have a long history of usage as thermometers for infrared detectors and their use for single photon calorimeters has many attractive features despite their being resistance devices which dissipate power when being read out. They can be manufactured with high sensitivities (large resistance change for a given temperature increase); they have high impedances which result in essentially negligible readout amplifier noise; and although their specific heat is higher than that of the pure semiconductor, they can be made extremely small by ion implantation of the dopant into small areas of the device. This latter approach also gets around the problem of attaching the thermometer to the detector. To date these are probably the most widely used and best understood types of thermometer for calorimeter readout.

One of the earliest demonstrations of calorimetry of single X-ray photons was by groups at the University of Wisconsin and NASA's Goddard Space Flight Center. Early results with a 0.25 × 0.25 mm silicon absorber at 0.3 K gave 270 eV energy resolution (McCammon *et al.*, 1984), and, at the time of writing, this has been considerably improved, to 7.3 eV FWHM, using a mercuric telluride absorber at 0.1 K (McCammon *et al.*, 1992) The absorber is bonded to a single slab of silicon which is etched away to form the necessary mechanical support bars and thermal links. Ion implantation of the silicon is used to form both the thermometer and the conductive tracks leading to it (McCammon *et al.*, 1987).

A spectrometer based on the single photon calorimeter is being developed for the focus of an imaging telescope. Originally intended for the AXAF-S mission, the X-Ray Spectrometer (XRS) will be an array of calorimeters of the type discussed above to provide imaging spectroscopy with greater than 90% efficiency up to 10 keV and response out to 20 keV. The projected energy resolution will be around 10 eV, the device will be operated at 65 milliKelvin, and each pixel, of which there will be around 30, will be $\frac{1}{4}$ mm^2 in area.

3.6. SUPERCONDUCTING TUNNEL JUNCTION DETECTORS

Finally, a class of detector in which there has been much interest lately is briefly described – the Superconducting Tunnel Junction (STJ). The attraction of this device is easy to understand; while the energy band gap in a semiconductor is 1 or 2 eV, that of a superconductor, below its critical temperature, is in the meV range and this directly translates into an energy resolution potentially $\approx$30 times better than for a silicon detector, or roughly equivalent to the calorimeter described above.

In a superconducting material the charge carriers exist in pairs, first identified by Cooper. These Cooper pairs can be broken up by photoelectrons (from X-ray interactions) to produce single charge carriers, termed quasiparticles, which can be made to tunnel out of the superconductor. Integrating this tunneling charge leads to a signal from the device (Gare *et al.*, 1989). A typical STJ detector would consist of two superconducting films separated by an insulating oxide layer through which the tunneling takes place. The energy resolution of such a device is dependent upon how much of the initial X-ray energy goes into breaking Cooper pairs, and how many of the resulting quasiparticles subsequently tunnel. A good fraction of the initial energy goes into phonons (thermal energy), but some of these, with energy above the band gap, can go on to break additional Cooper pairs. The initial energy loss then becomes due to those phonons below the band gap energy. Quasiparticles, once formed though, can also be lost, through recombination back to Cooper pairs, or by diffusion away from the tunneling area. Re-combination can be reduced by operating at temperatures well below the critical temperatures. All of these effects conspire to degrade the energy resolution from the theoretical figure given above.

Early results indicate that a large fraction of the quasiparticles are in fact lost from current detectors. STJs based on Sn and Nb superconductors have been tested with the best results, 50 eV energy resolution at 5.9 keV, coming from Sn (Zehnder *et al.*, 1990). Nb has so far delivered inferior results, around 100 eV (Hubner *et al.*, 1993), but is potentially more attractive due to a higher operating temperature (around 1K rather than 0.3 K). The devices for both materials tested to date ranged in size from 10 μm up to 0.5 mm. These early measurements have served to indicate the large potential of the STJ detector, but at the same time have shown that further work is needed to fully understand the quasiparticle loss mechanisms and hence to produce optimized devices.

4. Conclusions

The past few years have seen great changes in the instruments being developed for X-ray astronomy. These range from low-cost, lightweight optics to high-performance focal plane detectors such as CCDs, calorimeters, and superconducting tunnel junction detectors. In addition, progress has also been made with more traditional, large-area devices such as gas-filled counters. The next decade promises to be equally productive due to the potential for the development of X-ray optics for the hard X-ray region (20–100 keV), as well as room temperature semiconductors having high atomic numbers, such as cadmium telluride, which could provide energy resolutions approaching those currently obtained with high purity germanium detectors, but at the same time offer higher absorption efficiency, and ease of use. These technologies would then bring to the hard X-ray region the high sensitivity currently enjoyed at X-ray energies below 10–20 keV.

Acknowledgements

The authors wish to thank the members of the X-ray astronomy branch at MSFC for their help with this review. A special note of appreciation goes to Kurtis Dietz for his skill and hard work in generating the many figures contained herein.

References

Angel, J. R. P.: 1979, *Astrophys. J.* **233**, 364.

Aschenbach, B.: 1985, *Rep. Prog. Phys.* **48**, 579.

Aschenbach, B.: 1987, *SPIE* **830**, 152.

Austin, R. A., and Ramsey, B. D.: 1993, *Opt. Eng.* **32**, No. 8, 1990.

Austin, R. A., Minamitani, T., and Ramsey, B. D.: 1993, *SPIE* **2010**, 118.

Bateman, J. E.: 1984, *Nucl. Instr. Meth. Phys. Res.* **221**, 131.

Bertsch, D. L., Fichtel, C. E., and Trombka, J. I.: 1988, *Space Sci. Rev.* **48**, 113.

Blake, R. L., Chubb, T. A., Friedman, H., and Unzicker, A. E.: 1965, *Astrophys. J.* **142**, 1.

Bower, C. R., Dietz, K. L., Ramsey, B. D., and Weisskopf, M. C.: 1991, *IEEE Trans. on Nucl. Sci.* **38**(2), 585.

Bradt, H.V., Swank, J. H., and Rothschild, R. E.: 1990, *Adv. Space Res.* **10**(2), 297.

Brinkman, A. C., Dam, J., Mels, W. A., Skinner, G. K., and Willmore, A. P.: 1983, in G. C. Perola and M. Salvati (eds.), *Non-Thermal Processes and Very High Temperature Phenomena in X-Ray Astronomy*, Rome.

Budtz-Jorgensen, C., Bahnsen, A., Mohl Madsen, M., Olesen, C., and Schnopper, H. W.: 1992, *SPIE* **1743**, 162.

Canizares, C. R., and Kruper, J.: 1984, *Astrophys. J.* **278**, L99.

Cardini, D., Poulsen, J. M., Costa, E., Dal Fiume, D., Emanuele, A., Frontera, F., Basili, A., Franceschini, T., Frut, M., Landini, G., and Silvestri, S.: 1992, *Astron. Astrophys* **257**, 824.

Caroli E., Stephen, J. B., Di Cocco, G., Natalucci, L., and Spizzichino, A.: 1987, *Space Sci. Rev.* **45**, 349.

Casali, F., Bollini, D., Chirco, P., Rossi, M., Baldazzi, G., Dusi, W., Caroli, E., DiCocco, G., Donati, A., Landini, G., and Stephen, J. B.: 1992, *IEEE Trans. Nucl. Sci.* **NS-39**(4), 598.

Charpak, G., Bouclier, R., Bressani, T., Favier, J., and Zupancic, C.: 1968, *Nucl. Instr. Meth.* **62**, 262.

Charpak, G., Dominik, W., Santiard, J. C., Sauli, F., and Solomey, N.: 1989, *Nucl. Instr. Meth. Phys. Res.* **A274**, 275.

Chen, A., Kaaret, P., and Kenny, T. W.: 1993, *SPIE* **2011**, in press.

Christensen, F. E., Hornstrup, A., Westergaard, N. J., and Schnopper, H. W.: 1991, *SPIE* **1546**, 160.

Citterio, O., Conconi, P., Conti, G., Mattaini, E., Santambrogio, E., Cusumano, G., Sacco, B., Brauninger, H., and Burkert, W.: 1990, *SPIE* **1343**, 145.

Citterio, O., Conconi, P., Mazzoleni, F., Conti, G., Cusumano, G., Sacco, B., Brauninger, H., and Burkert, W.: 1991, *SPIE* **1546**, 150.

Citterio, O., Conconi, P., Ghigo, M., Mazzoleni, F., Brauninger, H., Burkert, W., Gondoin, P., van Katwijk, K., and Laurance, R.: 1992, *SPIE* **1742**, 256.

Covault, C. E.: 1991, PhD. Thesis, Harvard University.

Crannell, C. J., Dennis, B. R., Orwig, L. E., Schmahl, E. J., Lang, F. L., Starr, R., Norris, J. P., Greene, M. E., Hurford, G. J., Johnson, W. N., and Wood, K. S.: 1991, *AIAA International Balloon Technology Conference* **AIAA-91-3653**, 1.

Cruise, A. M., and Willmore, A. P.: 1975, *Monthly Notices Roy. Astron. Soc.* **170**, 165.

Dabrowski, A. J., Szymczyk, W. M., Iwanczyk, J. S., and Kusmiss, J. H.: 1983, *Nucl. Instr. Meth. Phys. Res.* **213**, 89.

de Korte, P. A., Giralt, R., Coste, J. N., Ernu, C., Frindel, S., Flamand, J., and Contet, J. J.: 1981, *Applied Optics* **20**(6), 1080.

de Korte, P. A. J., Bleeker, J. A. M., den Boggende, A. J. F., Branduardi-Raymont, G., Brinkman, A. C., Culhane, J. L., Gronenschild, E. H. B. M., Mason, I., and McKechnie, S. P.: 1981a, *Space Sci. Rev.* **30**, 495.

de Korte, P. A. J.: 1987, *SPIE* **830**, 172.

Dicke, R. H.: 1968, *Astrophys. J.* **153**, L101.

Dietz, K. L., Ramsey, B. D., and Weisskopf, M. C.: 1992, *SPIE* **1743**, 236.

Dietz, K. L., Ramsey, B. D., Weisskopf, M. C., and Austin, R. A.: 1993, *Proceedings of the AIAA Conference, 'Space Programs and Technologies'*, Huntsville.

Doxsey, R. E., Apparao, K. M. V., Bradt, H. V., Dower, R. G., and Jernigan, J. G.: 1977, *Nature* **269**, 112.

Elsner, R. F., Weisskopf, M. C, Novick, R., Kaaret, P., and Silver, E.: 1990, *SPIE* **1317**, 372.

Favata, F., and Smith, A.: 1989, *SPIE* **1159**, 488.

Fenimore, E. E.: 1978, *Applied Optics* **17**(22), 3562.

Fraser, G. W.: 1989, *Detectors in X-Ray Astronomy*, Cambridge University Press, New York.

Fraser, G. W., Pearson, J. F., and Lees, J. E.: 1987, *Nucl. Instr. Meth. Phys. Res.* **A256**, 410.

Fraser, G. W., Lees, J. E., Pearson, J. F., Sims, M. R., and Roxburgh, K.: 1991, *SPIE* **1546**, 41.

Fraser, G. W., Brunton, A. N., Lees, J. E., and Emberson, D. L.: 1993, *Nucl. Instr. Meth. Phys. Res.* **A334**, 579.

Fulton, M. A., Ramsey, B. D., and Kolodziejczak, J. J.: 1993, *SPIE* **2006**, in press.

Gaillardetz, R., Bjorkholm, P., Mastronardi, R., Vanderhill, M., and Howland, D.: 1978, *IEEE Trans. on Nucl. Sci.* **NS-25**(1), 437.

Gare, P., Engelhardt, R., van Dordrecht, A., Peacock, A., Lumley, J., Periera, C., Busfield, M., and Twerenbold, D.: 1989, *SPIE* **1159**, 433.

Garmire, G. P., Nousek, J., Burrows, D., Ricker, G., Bautz, M., Doty, J., Collins, S., Janesick, J., Mountain, R. W., Burke, B. E.: 1988, *SPIE* **982**, 123–128.

Garmire, G. P., Ricker, G. R., Bautz, M. W., Burke, B., Burrows, D. N., Collins, S. A., Doty, J. P., Gendreau, K., Lumb, D. H., and Nousek, J. A.: 1991, *AIAA Conference* **92**, 1473.

Gatti, E., and Rehak, P.: 1984, *Nucl. Instr. Meth. Phys. Res.* **A225**, 608.

Gehrels, N.: 1985, *Nucl. Instr. Meth. Phys. Res.* **A239**, 324.

Gehrels, N.: 1992, *Nucl. Instr. Meth. Phys. Res.* **A313**, 513.

Gehrels, N.: 1992a, Presented at Symposium on Photon Detectors in Space, ESTEC, November 10 –12, 1992.

Gendreau, K., Bautz, M., Ricker, G.: 1993, *Nucl. Inst. Meth. Phys. Res.*, in press.

Giacconi, R., Kellogg, E. M., Gorenstein, P., Gursky, H., and Tananbaum, H.: 1971, *Astrophys. J.* **165**, L27.

Gursky, H. and Zehnpfennig, T.: 1966, *Applied Optics* **5**(5), 875.

Gursky, H., Bradt, H., Doxsey, R., Schwartz, D., Schwarz, J., Dower, R., Fabbiano, G., Griffiths, R. E., Johnston, M., Leach, R., Ramsey, A., and Spada, G.: 1978, *Astrophys. J.* **223**, 973.

Heavens, O. S. and Liddell, H. M.: 1966, *Applied Optics* **5**(3), 373.

Henry, J. P., Kellogg, E. M., Briel, U. G., Murray, S., Van Speybroeck, L. P., and Bjorkholm, P. J.: 1977, *SPIE* **106**, 196.

Hubner, P., Rando, N., Peacock, A., Videler, P., van Dordrecht, A., and Lumley, J.: 1993, European Space Agency Reprint No. ESLAB 93/169.

Hudson, H. S.: 1985, *NASA Conference Publication* **2421**, 5.

Joensen, K. D., Hoghoj, P., Christensen, F., Gorenstein, P., Susini, J., Ziegler, E., and Wood, J.: 1993, *SPIE* **2011**, in press.

Joyce, R. M., Becker, R. H., Birsa, F. B., Holt, S. S., and Noordzy, M. P.: 1978, *IEEE Trans. on Nucl. Sci.* **NS25**(1), 453.

Kaaret, P., Geissbuhler, P., Chen, A., and Glavinas, E.: 1992, *Applied Optics* **31**, 7339.

Kaaret, P., Schwartz, J., Soffita, P., Dwyer, J., Shaw, P., Hanany, S., Novick, R., Sunyaev, R., Lapshov, I., Silver, E., Ziock, K. P., Weisskopf, M. C., Elsner, R. F., Ramsey, B. D., Costa, E., Rubini, A., Feroci, M., Piro, L., Manzo, G., Giarrusso, S., Santangelo, S., Scarsi, L., Perola, G. C., Massaro, E., and Matt, G.: 1993, *SPIE* **2011**, in press.

Kestenbaum, H. L., Long, K. S., Novick, R., Weisskopf, M. C., and Wolff, R. S.: 1977, *Astrophys. J.* **216**, L19.

Knoll, G. F.: 1989, *Radiation Detection and Measurement*, Second Edition, John Wiley and Sons, New York.

Kumakhov, M. A.: 1990, *Nucl. Instr. Meth. Phys. Res.* **B48**, 283.

Markert, T. H, Powers, T. R., Levine, A. M., McCullum, C. B., Mohr, J. J., and Canizares, C. R.: 1988, *SPIE* **982**, 245.

McCammon, D., Moseley, S. H., Mather, J. C., and Mushotzky, R. F.: 1984, *J. Appl. Phys.* **56**, 1263.

McCammon, D., Juda, M., Zhang, J., Holt, S. S., Kelley, R. L., Moseley, S. H., and Szymkowiak, A. E.: 1987, *Japanese J. Applied Phys.* **26**, 2084.

McCammon, D., Cui, W., Juda, M., Morgenthaler, J., Zhang, R., Kelley, R. L., Holt, S. S., Madjeski, G. M., Moseley, S. H., and Szymkowiak, A. E.: 1992, *Proc. 6th European Symposium on Semiconductor Detectors*, Milan.

Meszaros, P., Novick, R., Chanan, G. A., Weisskopf, M. C., and Szentgyorgyi, A.: 1988, *Astrophys. J.* **324**, 1056.

Murray, S. S., Chappell, J. H., Elvis, M. S., Forman, W. R., Grindlay, J. E., Harndeniana, G. S., Pounds, K. A., Fraser, G. W., and Henry, J. P.: 1987, *Astrophys. Letters and Communications* **26**, 113.

Oda, M.: 1965, *Applied Optics* **4**, 143.

Ogawara, Y., Mitsuda, K., Masai, K., Vallerga, J. V., Cominsky, L. R., Grunsfeld, J. M., Kruper, J. S., and Ricker, G. R.: 1982, *Nature* **295**, 675.

Ohashi, T., Makishima, K., Ishida, M., Tsuru, T., Tashiro, M., Mihara, T., Kohmura, Y., and Inoue, H.: 1991, *SPIE* **1549**, 9.

Peacock, A., Andresen, R. D., Manzo, G., Taylor, B. G., Villa, G., Re, S., Ives, J. C., and Kellock, S.: 1981, *Space Sci. Rev.* **30**, 525.

Petre, R., and Serlemitsos, P.J.: 1985, *Applied Optics* **24**(12), 1833.

Pfeffermann, E., Brial, U. G., Hippmann, H., Kettenring, G., Metzner, G., Predehl, P., Reger, G., Stephan, K. H., Zombeck, M. V., Chappell, J., and Murray, S. S.: 1986, *SPIE* **733**, 519.

Policarpo, A. J. P. L., Alves, M. A. F., Dos Santos, M. C. M., and Carvalho, M. J. T.: 1972, *Nucl. Instr. Meth. Phys. Res.* **102**, 337.

Proctor, R. J., Skinner, G. K., and Willmore, A. P.: 1978, *Monthly Notices Roy. Astron. Soc.* **185**, 745.

Ramsey, B. D. and Agrawal, P. C.: 1988, *SPIE* **982**, 258.

Ramsey, B. D. and Agrawal, P. C.: 1989, *Nucl. Instr. Meth. Phys. Res.* **A278**, 576.

Ramsey, B. D. and Weisskopf, M. C.: 1987, *IEEE Trans. on Nucl. Sci.* **NS34**(3), 672.

Ramsey, B. D., Bower, C. R., Dietz, K. L., and Weisskopf, M. C.: 1990, *SPIE* **1344**, 82.

Ramsey, B. D.: 1992, *SPIE* **1743**, 96.

Rossington, C. S., Giauque, R. D., and Jaklevic, J. M.: 1992, *IEEE Trans. Nucl. Sci.* **NS-39**(4), 570.

Sadoulet, B., Edberg, T. K., Weiss, S., Parsons, A., Wilkerson, J., Hurley, K., Lin, R. P., and Smith, G.: 1989, *SPIE* **1159**, 45.

Samson, J. A. R.: 1967, *Techniques of Vacuum Ultraviolet Spectroscopy*, John Wiley and Sons, Inc., New York.

Schattenburg, M. L., Canizares, C. R., Dewey, D., Levine, A. M., Markert, T. H., and Smith, H. I.: 1988, *SPIE* **982**, 210.

Schnopper, H. W., Thompson, R. I., and Watt, S.: 1968, *Space Sci. Rev.* **8**, 534.

Schnopper, H. W., Van Speybroeck, L. P., Delvaille, J. P., Epstein, A., Källne, E., Bachrach, R. Z., Dijkstra, J., Lantward, L.: 1977, *Applied Optics* **16**(4), 1088.

Seigmund, O. H. W., Clothier, S., Thornton, J., Lemen, J., Harper, R., Mason, I. M., Culhane, J. L.: 1983, *IEEE Trans. on Nucl. Sci.* **30**(1), 503.

Serlemitsos, P. J., Petre, R., Glasser, C., Birsa, F.: 1984, *IEEE Trans. Nucl. Sci.* **NS-31**(1), 786.

Seward, F. D., Chlebowski, T., Delvaille, J. P., Henry, J. P., Kahn, S. M., Van Speybroeck, L. Van, Dijkstra, J., Brinkman, A. C., Heise, J., Mewe, R., Schrijver, J.: 1982, *Applied Optics* **21**(11), 2012.

Simons, D. G., de Korte, P. A. J., Peacock, A., and Bleeker, J. A. M.: 1985, *SPIE* **597**, 190.

Sipila, H., Huttunen, P., Kämäräinen, V. J., Vilhu, O., Kurki, J., Leppelmeier, G. W., Taylor, I., Niemelä, A., Lægsgaard, E., Sunyaev, R.: 1991, *SPIE* **1549**, 246.

Skinner, G. K.: 1984, *Nucl. Instr. & Meth. in Phys. Res.* **221**, 33.

Swinyard, B.M., Malaguti, G., Caroli, E., Dean, A. J., and Di Cocco, G.: 1991, *SPIE* **1548**, 94.

Sze, M.: 1985, *Semiconductor Devices, Physics and Technology*, Wiley and Sons, Inc., New York.

Tueller, J.: 1990, *Astrophys. J.* **351**, L41.

Turner, M. J. L., Thomas, H. D., Patchett, B. E., Reading, D. H., Makishima, K., Ohashi, T., Dotani, T., Hayashida, K., Inoue, H., Kondo, H., Koyama, K., Mitsuda, K., Ogawara, Y., Takano, S., Awaki, H., Tawara, Y., and Nakamura, N.: 1989, *Publ. Astron. Soc. Japan* **41**, 345.

Ubertini, P., Bazzano, A., Boccaccini, L., Federici, M., Frutti, M., Gianni, G., Manzan, M., Patriarca, R., Soggiu, M. E., and Ugazio, S.: 1990, *SPIE* **1344**, 479.

Ubertini, P., Bassani, L., Bazzano, A., Lund, N., Manzo, G., Mas, M., Smith, A., Soggiu, E. Staubert, R., and Turner, M.: 1993, *Astron. Astrophys. Suppl.* **97**, 389.

Ulmer, M. P.: 1989, *SPIE* **1160**, 426.

Vallerga, J. V., Ricker, G. R., Schnepple, W. S., and Ortale, C.: 1982, *IEEE Trans. Nucl. Sci.* **NS-29**(1), 151.

Van Speybroeck, L. P.: 1987, *Astrophys. Letters and Communications* **26**(1–2), 127.

Walker, A. B. C., Barbee, T. W., Hoover, R. B., and Lindblom, J. F.: 1988, *Science* **241**, 1725.

Watkins, R. B. and Kaaret, P. E.: 1990, *SPIE* **1344**, 74.

Westergaard, N. J., Byrnak, B. P., Christensen, F. E., Grundsee, P., Hornstrup, A., Henrichsen, U., Jespersen, E., Norgaard-Nielsen, H. U., Polny, J., Schnopper, H. W., and Orup, P.: 1990, *Optical Engineering* **29**(6), 658.

Weisskopf, M. C., Silver, E. H., Kestenbaum, H. L., Long, K. S., and Novick, R.: 1978, *Astrophys, J.* **220**, L117.

Weisskopf, M. C.: 1992, *SPIE* **1742**, 2.

Wells, A., Stewart, G. C., Turner, M. J. L., Watson, D. J., Whitford, C. H., Antonello, E., Citterio, O., Brauninger, H., Cropper, M. S., Curtis, W. J., Peskett, S., Eyles, C. J., Goodall, C. V., Mineo, T., Sacco, B., and Terekhov, O.: 1991, *SPIE* **1546**, 205.

Wilkins, S. W., Stevenson, A. W., Nugent, K. A., Chapman, H., and Steenstrup, S.: 1989, *Rev. Sci. Instr.* **60**(6), 1026.

Wilkinson, D. H.: 1950, *Ionisation Chambers and Counters*, Cambridge University Press, Cambridge.

Willmore, A. P., Skinner, G. K., Eyles, C. J., and Ramsey, B. D.: 1984, *Nucl. Instr. Meth.* **221**, 284.

Zarnecki, J. C. and Culhane, J. L.: 1977, *Monthly Notices Roy. Astron. Soc.* **178**, 57.

Zehnder, A., Hagen, C. W., and Rothmund, W.: 1990, *SPIE* **1344**, 286.

Zombeck, M. V.: 1990, *Handbook of Space Astronomy and Astrophysics*, Cambridge University Press, Cambridge.